Journal Home Page: https://sjes.univsul.edu.iq/

Research Article:

Role of Geometrical Parameters on Heat Transfer in Liquid-Solid Fluidized Beds

Sherko Ahmad Flamarz Al-Arkawazi [a,*]
[a] **Garmian Polytechnic University, Kalar Technical College, Electrical & Computer department,KR,Iraq**

Article Information

Article History:
Received: January, 20th 2026
Accepted : March 21, 2026
Available online: April, 2025

Keywords:
Heat transfer; Fluidization; Packed beds; Column diameter.

About the Authors:
Corresponding author:
SherkoAhmad Flamarz Al-Arkawazi
E-mail: sherko.flamarz@gpu.edu.iq

DOI https://doi.org/10.17656/sjes.10210

Abstract

A numerical investigation of hydrodynamic and heat transfer characteristics in liquid-solid fluidized beds was conducted using a coupled CFD-DEM approach combined with a thermal model. Simulations were carried out for a range of particle and column diameters with varying inlet fluid velocities under isothermal wall boundary conditions. The model was capable of simulating the simultaneous effects of conductive particle-particle heat transfer and convective particle-fluid heat transfer. The accuracy of the coupled model was established by validating the results against experimental data in the literature on hydrodynamic characteristics and thermal behavior. It has been observed that the results obtained from the CFD-DEM simulation have a good agreement with the experimental data, and the average deviation is within the range of 6-8%. From the results, it was evident that the smaller particles improved the heat transfer performance. Enhancements of convective heat transfer and a decrease of temperature gradients in the bed with increasing inlet fluid velocity were found, especially in the column with the wider diameter. Results from the simulations elucidated the conductive heat transfer through contacts between particles as well as the convective heat transfer between fluid and particles, and showed that the interplay between particle size, column diameter, and fluid velocity determines the performance of heat transfer. The novelty in this research is the quantification of conduction and convection heat transfer interactions using a fully resolved CFD-DEM model for heat transfer. This research also gives practical guidelines on how to improve heat transfer in liquid-solid fluidized bed reactors by optimizing particle sizes and column diameters. The findings provide guidance for optimizing column geometry and particle size in fluidized bed reactors for enhanced thermal efficiency in chemical processing and thermal processing equipment.

1. Introduction

Liquid-solid fluidized beds have found wide use in chemical processing, biochemical engineering, and thermal energy storage systems because of their improved heat and mass transfer characteristics and good mixing behavior [1-5]. Heat transfer efficiency in these systems is highly controlled by the hydrodynamics and thermal interactions of the liquid and solid phases, which are further controlled by a number of operational and geometric parameters, most importantly particle size, column diameter, fluid velocity, and thermal boundary conditions [6,7].

Among these parameters, the diameter of the particle has a determining influence on the interfacial area for heat exchange, particle inertia, and bed height behavior. Smaller particles provide a larger surface area to volume ratio, a greater tendency for particle entrainment and elutriation, which promotes enhanced fluid-solid heat transfer and improved temperature uniformity throughout the bed [8]. These advantages are generally obtained at the cost of higher pressure drops and channeling effects [9, 10]. Larger particles lead to better bed stability and less entrainment but generally cause lower heat transfer rates because of worse contact between fluid and particle phases [11, 12]. Likewise, the inner diameter of the column has a strong impact on wall effects, radial heat distribution, and flow patterns. Narrow columns can facilitate radial conduction via enhanced

particle-wall contact but possibly inhibit bulk circulation, while wider columns provide improved fluidization quality and homogeneity at the expense of larger thermal gradients and weaker wall influence [13-15].

On the other hand, column diameter has a direct influence on wall effects, bed expansion, particle distribution, and flow uniformity. Small column diameters are frequently characterized by pronounced wall effects, which change local fluid velocities and particle residence times and, therefore, radial heat transfer distribution and axial dispersion [16, 17]. While larger diameters are likely to have more uniform fluidization behavior but can be prone to channeling or poor contact between phases if not duly optimized [18]. Experimental studies by David and Liang-Shih [19] and Chen et al. [20] have shown a strong dependence of local heat transfer coefficients on the fluidization column geometry. While experimental studies have yielded fundamental knowledge of such effects, they are constrained in resolving micro-scale heat transfer mechanisms and transient particle-scale interactions.

Over the past decade, the coupled computational fluid dynamics and discrete element method (CFD-DEM) strategy has developed into an effective means of studying fluidized systems. The approach resolves the fluid flow using continuum equations while concurrently tracking the movement and interaction of discrete particles, facilitating particle-scale resolution of momentum and energy transfer prediction [21-24]. The CFD-DEM paradigm has been used successfully to replicate intricate multiphase flow behavior and examine conduction, convection, and radiation heat transfer in fluidized settings [25, 26]. The CFD-DEM presents a sophisticated platform to investigate the granular dynamics and thermal transport behavior at the particle scale [27]. CFD-DEM enables the explicit resolution of single particle motion and fluid-particle interactions, which facilitates more precise prediction of local and global heat transfer characteristics. In comparison to conventional empirical or averaged Eulerian models, CFD-DEM resolves particle-scale interactions, allowing for in-depth examination of micro-scale phenomena like near-wall effects, particle clustering, and heat conduction paths [28-32]. The recent studies have shown the capability of the CFD-DEM technique for simulating the hydrodynamics and heat transfer in fluidized beds, including the particle temperature distribution, local heat transfer coefficient, etc. [33].

De Munck et al. [34] established a high-fidelity CFD-DEM model in order to capture near-wall thermal gradients in fluidized and packed beds. They highlighted the necessity of resolving the thermal boundary layer in the vicinity of the wall, whose thickness is of the order of a single particle diameter. In addition, coarse-grained CFD-DEM formulations have been proposed to save computational expense while maintaining accurate macroscopic thermal behavior, especially for larger-scale systems [35].

CFD-DEM research has demonstrated that reducing particle size enhances thermal exchange owing to higher contact area and improved particle mixing. This advantage is, however, offset by operational issues like heightened cohesion, particle agglomeration, and fluidization instability upon utilization of very fine particles. Additionally, particle size influences tend to be interdependent on system parameters such as superficial velocity, bed geometry, and particle material properties, making it difficult to interpret isolated trends [36]. Particle size has been widely recognized as a key factor in controlling the balance between conduction and convection in fluidized beds. In more recent studies, the influence of particle shape and structural properties on heat transfer performance has been investigated. For example, in CFD-DEM simulations carried out on fluidized beds in dryers, where ellipsoidal particles were used, it was found that the shape of the particles influenced the hydrodynamic and heat transfer performance because of changes in the drag forces and Reynolds number [33]. Moreover, numerical simulations carried out on spout fluid beds showed that different flow regimes have a significant impact on temperature profiles and heat transfer mechanisms [37]. Alipoor et al. [38] carried out a parametric CFD-DEM analysis of the influence of particle size and fluidization regime on thermal transport. Their findings illustrated that in the bubbling regime, larger particles improved convective heat transfer as a result of higher porosity (voidage) and fluid mixing. Particle-fluid-particle conduction was, however, reduced because of the larger interstitial spaces. Smaller particles were shown to facilitate more uniform temperature distribution and improved conductive pathways in dense beds, in agreement with previous results in packed beds [39]. Mu et al. [40] simulated a pseudo-2D CFD-DEM heat transfer in beds of different particle sizes subjected to constant wall heating. The addition of internal particle heat generation enabled the authors to more realistically analyze thermal response. They concluded that smaller particles resulted in quicker thermal response and improved heat penetration within the bed. In addition to the particle properties, geometrical parameters of the fluidized bed reactor have been recognized as important factors that affect the hydrodynamics and heat transfer in the fluidized beds. The geometrical parameters of the fluidized bed reactor include the design features, such as the diameter and height of the column, and the presence of internal structures and walls in the reactor, which

may affect the hydrodynamics and heat transfer in the fluidized beds. For instance, it has been found that changes in the geometrical parameters, such as ribbed walls in the reactor, can enhance heat transfer by improving the mixing and turbulence in the particles in the fluidized beds [41]. Column geometry, particularly the internal diameter, has a strong impact on hydrodynamics and heat transfer in fluidized beds. Wall effects dominate in small-diameter columns, resulting in non-uniform flow, high pressure drops, and changed minimum fluidization velocities. Studies on the fluidization of particles in a liquid in a narrow tube, known as a solid-liquid fluidized bed, have revealed that geometrical confinement can cause the particles to cluster or jam, thereby affecting the hydrodynamic structures and, in turn, the heat transfer process itself [42]. Xu et al. [43] used CFD-DEM to study the effect of column diameter and bed height on fluidization behavior for Geldart B particles. They noted that wall effects inhibited bubble formation and raised the minimum fluidization velocity in narrow columns. The geometric constraints involved have a profound impact on the nature of heat transfer. In smaller columns, a higher surface area to volume ratio enhances heat conduction via the walls, but this can lead to flow channeling and local overheating. Larger columns allow a more developed flow, reducing the wall effect and thus promoting radial temperature uniformity [1].

Fluid velocity and inlet temperature also play a vital role in controlling the thermal and hydrodynamic behavior. High flow velocity generally augments convective transport owing to increased particle-fluid interaction and mixing, whereas higher fluid temperatures affect viscosity and thermal diffusivity, modifying the local and global heat transfer rates [21]. Furthermore, the heat-transfer coefficient was very sensitive to inlet velocity, especially in the vicinity of the fluidization threshold.

Although past research has concentrated on either general hydrodynamics or overall heat transfer performance, a detailed numerical investigation accounting for particle-scale behavior and thermal transport mechanisms as a function of column diameter and particle size on the heat transfer performance is still lacking. The previous studies have neglected the combined influence of column diameter and particle size. Therefore, the current research seeks to fill this research gap by utilizing a CFD-DEM coupled methodology, combined with a thermal model, to explore the influence of column inner diameter on heat transfer in a liquid-solid fluidized bed for different operational and geometrical conditions.

The present work uses the CFD-DEM approach combined with a thermal model, which will help to empower researchers with a complete framework to analyze such systems, aiding in the optimization of these processes and improving the performance of heat transfer in fluidization processes across a range of industrial applications. The novelty of this study investigates the influences of combining the parameters of particle size, column size, and inlet liquid velocity on heat transfer performance under well-controlled thermal and hydrodynamic conditions within liquid-solid fluidized beds. Therefore, the general objectives are; 1) investigate the effect of particle size by using three different diameters (2, 3, 5 mm), on local and average heat transfer via a CFD-DEM coupled in liquid-solid fluidized beds, 2) assess the role of column inner diameter for two column diameters (51 and 96 mm) on the development of flow regimes and heat transfer efficiency under the same fluidization conditions, 3) explore the influences of combining the effect of particle size and column diameter on hydrodynamics and thermal transport processes for a range of inlet fluid velocities (0.08-0.20 m/s), 4) offer detailed visualization and analysis of the heat energies (conduction and convection), and particle motion that lead to the heat transfer variations to develop the liquid-solid fluidized beds.

2. Methods and Materials

To examine the effect of particle size and column diameter on heat transfer in liquid-solid fluidized beds, a coupled (CFD-DEM) methodology is used. The fluid phase was represented in the Eulerian (CFD) framework by the solution of the Navier-Stokes equations, and the solid phase was represented by Lagrangian (DEM) particle tracking based on Newton's laws of motion. Heat transfer among the fluid, particles, and wall boundaries was included by suitable thermal coupling models, and simulations were implemented using CFD-DEM coupling [44, 45].

2.1Eulerian fluid phase (CFD approach)

The Eulerian computational platform has been established by using the Salome platform and the CFD (Code_Saturne), which is developed by France's electricity (EDF). The fluid phase is modeled by Reynolds-averaged Navier-Stokes equations with the standard (k-ε) turbulence model. The (k-ε) is one of the most common two-equation models for simulating turbulent flows in computational fluid dynamics (CFD). Introduced by Launder and Spalding **[**46**]**, it uses two distinct transport equations: one for turbulent kinetic energy (k) and another for its dissipation rate (ε). The (k-ε) is based on the Boussinesq hypothesis for Reynolds stresses. The mass, momentum, and turbulence transport equations **[**46**]** are:

- Continuity equation:

$$\frac{\partial \rho_f}{\partial t} + \nabla \cdot (\rho_f v_f) = 0 \quad (1)$$

-Momentum equation:

$$\frac{\partial}{\partial t}(\rho_f v_f) + \nabla \cdot (\rho_f v_f v_f) = -\nabla p + \nabla \cdot \tau_f + \rho_f g + F_{fs} \quad (2)$$

-Turbulent Stress equation:

$$\tau_f = \mu_{eff}(\nabla v_f + \nabla v_f^T) - \frac{2}{3}\mu_{eff}(\nabla \cdot v_f) I \quad (3)$$

$$where \quad \mu_{eff} = \mu_f + \mu_t \quad and \quad \mu_t = C_\mu \rho_f \frac{k^2}{\varepsilon}$$

-Turbulent Kinetic Energy equation:

$$\frac{\partial}{\partial t}(\rho_f k) + \nabla \cdot (\rho_f v_f k) = \nabla \cdot \left(\left(\mu_f + \frac{\mu_t}{\sigma_k} \right) \nabla k \right) + P_k - \rho_f \varepsilon \quad (4)$$

-Turbulent Dissipation Rate equation:

$$\frac{\partial}{\partial t}(\rho_f \varepsilon) + \nabla \cdot (\rho_f v_f \varepsilon) = \nabla \cdot \left(\left(\mu_f + \frac{\mu_t}{\sigma_\varepsilon} \right) \nabla \varepsilon \right) + C_{1\varepsilon} \frac{\varepsilon}{k} P_k - C_{2\varepsilon} \rho_f \frac{\varepsilon^2}{k} \quad (5)$$

-Turbulent viscosity:

$$\mu_t = \rho_f C_\mu \frac{k^2}{\varepsilon} \quad (6)$$

Where ρ_f is fluid density, v_f is fluid velocity, and p is fluid pressure, τ_f is viscous stress, F_{fs} refer to external forces, μ_f is fluid viscosity, μ_{eff} is effective viscosity, μ_t is turbulent viscosity, and P_k is production of turbulent kinetic energy. The value of each constant in the above equations is; C_μ=0.09, σ_k=1.0, σ_ε=1.3, $C_{1\varepsilon}$=1.44, $C_{2\varepsilon}$=1.92.

The geometric model was created in Salomé, which is an open source software platform, where the boundary conditions were also defined, and then meshing was discretized to unstructured tetrahedral elements, providing a generic Pre- Processing and Post-Processing environment for numerical simulation. The meshes independent are tested in previous work [44]. For each particle, the interaction force between fluid and solid is determined, which is the drag force. While Code_Saturne is utilized as a solver addressing the RANS (Reynolds-Averaged Navier-Stokes) equations for incompressible mean flow by employing a finite volume discretization method, the CFD code is based on a co-located finite volume approach that accepts meshes with any type of cell for calculations of the fluid flow [47].

2.2 Lagrangian particle phase (DEM approach)

The DEM code (software) was developed in our lab [44]. The Solid phase (particles) was modeled based on the premises considered in the present work. Assume that the particles are considered as rigid during the entire simulation time, a hard sphere model, and the contact between two adjacent particles. The DEM is initiated and developed by Cundall and Strack [48]. The DEM offers the possibility of numerically modeling kinematic and dynamic effects induced by a large number of interacting particles. In this work, the DEM solver uses the Non-Smooth Contact Dynamics (NSCD) algorithm, which is used for short contact to treat the particles. The NSCD was initiated and developed by Jean and Moreau [49]. The method for solving the frictional unilateral conditions is based on the bi-potential theory [50], which uses partitioning coupled with a table of connectivity [51], which makes it possible to considerably reduce the calculation time. The method of bi-potential works on the principle of prediction and correction.

In DEM, the particles are assumed to be discrete, interacting particles that obey Newton's second laws of motion. The technique simulates the path of every particle separately by calculating the forces and torques exerted on it by particle-particle and particle-wall interactions. Each solid particle's motion has two types of motion: translation and rotation, which are expressed as:

-Translational motion:

$$m_p \frac{du_p}{dt} = \sum_{j=1}^{nc} F_{c,ij} + F_{B,p} + m_p g + F_{fp} \quad (7)$$

-Rotational motion:

$$I_p \frac{d\omega_p}{dt} = \sum_{j=1}^{nc} T_{c,ij} + T_{fp} \quad (8)$$

Where m_p is the mass of the particle, n_c is the number of particles j candidate to contact with particle i, F_c, T_c are the contact force and torque of particle, contact forces use the Hertz-Mindlin contact model, the particle-particle and particle-wall interactions were controlled using the Hertz-Mindlin [52] contact model with rolling friction, $F_{B,p}$ is buoyant force, g is gravity acceleration, and F_{fp}, T_{fp} are fluid-particle interaction force (drag force) and torque.

In this study, focus will not be on exploring the

multitude of theories in depth; rather, it will center attention on Hertz's widely acknowledged theory. Consider the situation involving two rigid objects being pressed together by a perpendicular contact force. Initially, these solids make contact at a single point, which then evolves into a contact surface as a result of deformation. In this research, the particle postulates will be founded on Hertz's theory; therefore, (*i*) the contact surface is both continuous and conformal, (*ii*) the deformations are minor and elastic, (*iii*) the contact force is static, and (*iv*) the materials of the objects are isotropic and homogeneous.

2.3Coupling CFD-DEM

The coupling CFD-DEM applied in this work is based on a simple standard one-way coupling approach, which uses a CFD calculation for the fluid phase, while applying the DEM code for the solid phase. The interphase momentum exchange between the fluid and the solid (drag force) is ascertained for each particle.

2.4 Interphase momentum exchange

Interphase momentum transfer in liquid-solid fluidized beds refers to the interaction of momentum between the liquid and solid particles, which is crucial for regulating the dynamics of fluidization [53]. This interaction is quantified by interphase drag forces, which act as source terms in the momentum equations of the two-phase system. Essentially, it describes the way in which the fluid influences the acceleration or deceleration of the particles, and vice versa. In this work, the Syamlal and O'Brien drag force model [54] is utilized. The Syamlal and O'Brien drag law is:

$$C_{Ds} = \left[0.63 + \frac{4.8}{\sqrt{\mathrm{Re}_{ts}}} \right]^2 \tag{9}$$

$$\mathrm{Re}_{ts} = \left[\frac{4.8^2 + 2.52\sqrt{\frac{4Ar}{3}} - 4.8}{1.26} \right]^2$$

$$and \quad Ar = \frac{\rho_f}{\mu_f^2} d_p^3 \left(\rho_p - \rho_f\right) g \tag{10}$$

Where C_D is the drag coefficient for a single particle, Re_{ts} is the Reynolds number for terminal velocity for a single particle, and Ar is the Archimedes number.

The model is a popular empirical correlation for estimating the interphase momentum transfer between particles and fluid in gas-solid and liquid-solid multiphase flows. The interphase drag force is modeled using the Syamlal and O'Brien model:

$$F_{fp} = K_{fp}(u_p - v_f) \tag{11}$$

However, Syamlal and O'Brien model adjusted this with a correction factor that accounts for the porosity of fluid (ε_f);

$$K_{fp} = \frac{3C_D \varepsilon_f \rho_f \left|v_f - u_p\right|}{4 d_p} \tag{12}$$

$$C_D = \frac{24}{\mathrm{Re}_p}\left(1 + 0.15\,\mathrm{Re}_p^{\,0.687}\right) \cdot \varepsilon_f^{-2.65}$$

$$and \quad \mathrm{Re}_p = \frac{\rho_f d_p \left|v_f - u_p\right|}{\mu_f} \tag{13}$$

Where d_p, u_p, and Re_p represent diameter, translational velocity, and Reynolds number for the particle, and C_D is the fluid drag coefficient.

3. Heat Transfer Modeling

The heat transfer processes in liquid-solid fluidized beds are affected by complex interactions between the ongoing liquid phase, the individual solid particles, and the column's walls. In the current CFD-DEM approach, heat transport is represented by solving the heat transfer equations applicable to the fluid and particle phases, encompassing conduction, convection, and interactions between particles and the wall [55]. The radiation heat transfer gains significance as temperature rises and can completely dominate conduction and convection at extremely high temperatures. It is commonly accepted that radiation flux becomes the primary mode of heat transfer when temperatures exceed 400 °C [56], which is not applicable in the current study. When a temperature difference is present within a solid material, the process of heat transfer is referred to as conduction. This transfer mechanism arises from interactions at the atomic or molecular scale. Although this phenomenon is also observable in fluids, it is typically overshadowed by convection. In the case of a granular medium, this is described as a system featuring several points of interaction [57]. In the thermal conductance modeling, it is presumed that particles do not exhibit any temperature gradient, assigning a single temperature to each particle. This simplification can be deemed valid when the ($Bi \ll 0.1$) where Bi is the Biot number, which is a dimensionless parameter that compares internal conductive resistance in a solid particle to external convective resistance with the surrounding fluid. It is defined by a specific relationship [58-60]. The Biot number for spherical particles:

$$Bi = \frac{h_{p,f} d_p}{2\lambda_p} \tag{14}$$

Where $h_{p,f}$ is the convective heat transfer coefficient

between the particle and the fluid, and λ_p is the thermal conductivity of the solid material (particle). The formulations of conduction involving particle-particle, and particle-fluid-particle are detailed as; conduction particle-particle [56]:

$$Q_{Cond.p-p} = H_C\left(T_{p,i} - T_{p,j}\right)$$
$$and \quad H_C = \frac{4a}{\frac{1}{\lambda_{p,i}} + \frac{1}{\lambda_{p,j}}} \tag{15}$$

Where $T_{p,i}$ and $T_{p,j}$ represent the temperatures at the centers of the particles, while H_C denotes the conductance coefficient, and a is the radius of contact. The contact point of particle-particle mark circular contact area, according to Hertz theory, the radius of contact for the same material and particle size.

$$= \left(\frac{3F_{C,n}r^*}{4E^*}\right)^{\frac{1}{3}} \quad , \quad \frac{1}{E^*} = \frac{2\left(1-\nu_p^2\right)}{E_p} \tag{16}$$
$$, \quad and \quad \frac{1}{r^*} = \frac{2}{r_p}$$

Where $F_{C,n}$ is the normal force, r^* is equivalent radius, ν_p Poisson's ratio, and E^* is an equivalent Young's modulus.

Conduction particle-fluid-particle is the second part of the thermal conduction, which details the interaction of heat between particles and the fluid. It introduces a framework utilizing finite volume elements. The system is segmented into rectangular elements, where each element may include varying quantities of particles or segments of an article [57]:

$$Q_{Cond.p-f-p} = m_f C_{p,f}\left(\frac{T_{i,j}^{t+\Delta t} - T_{i,j}^{t}}{\Delta t} + \right.$$
$$v_{fx}\frac{T_{i+1,j}^{t} - T_{i-1,j}^{t}}{2\Delta x} + v_{fy}\left.\frac{T_{i,j+1}^{t} - T_{i,j-1}^{t}}{2\Delta y}\right) - \lambda_f S_p \tag{17}$$
$$\left(\frac{T_{i+1,j}^{t} - T_{i,j}^{t} + T_{i-1,j}^{t}}{\Delta x^2} + \frac{T_{i,j+1}^{t} - T_{i,j}^{t} + T_{i,j-1}^{t}}{\Delta y^2}\right)$$

where m_f, $C_{p,f}$, and λ_f represent the fluid mass, the heat capacity, the thermal conductivity of fluid, and the $T_{i,j}$ temperature of the fluid, it is assumed to remain uniform within each element, while v_{fx} and v_{fy} are the fluid velocity components in x- and y- directions in each element, and S_p represents the surface of the particle that is in contact with the fluid within the element.

Convection heat transfer serves as the primary mechanism in liquid-solid fluidized beds, where an upward-flowing continuous liquid phase moves through a suspended solid particle bed. This process significantly influences the thermal exchange between the heating surfaces or walls and both the fluid and solid particles, which is crucial for the overall thermal efficiency of the system [58, 59]. In such a system, heat transfer primarily results from forced convection, which arises from the movement of the fluid and solid particles. The disruption of the thermal boundary layer is enhanced as the liquid flows through the gaps between the fluidized particles, leading to improved local and average heat transfer coefficients. The degree of turbulence among the particles and their interaction with the fluid is highly sensitive to various operational parameters, such as superficial fluid velocity, particle size and density, and the geometry of the column. The convective heat transfer can be expressed mathematically according to Newton's law:

$$Q_{Conv.} = h_{p,f} S_p (T_{p,i} - T_f) \tag{18}$$

For a single particle, the heat transfer coefficient is obtained from a Nusselt number correlation.

$$Nu_p = \frac{h_{p,f} d_p}{\lambda_f} \tag{19}$$

The particle Nusselt number Nu_p is obtained from the empirical correlation by Gunn [60] for packed and fluidized beds for gas and liquid of particles within the Reynolds number (1-10^5) and porosity range (0.35-1);

$$Nu_p = (7 - 10\varepsilon_f + 5\varepsilon_f^2)(1 + 0.7\,\mathrm{Re}_p^{0.2}\,\mathrm{Pr}^{0.33})$$
$$+ (1.33 - 2.4\varepsilon_f + 1.2\varepsilon_f^2)\,\mathrm{Re}_p^{0.7}\,\mathrm{Pr}^{0.33} \tag{20}$$

Where $\mathrm{Pr} = \frac{\mu_f C_{p,f}}{\lambda_f}$, Pr is the Prandtl number, and μ_f is fluid viscosity. Integrating equations 15, 17, and 18 in the DEM code (energy balance equation (21)), where the thermal transfer behavior for particle i, considering its interactions with γ neighboring particles,

$$m_{p,i} C_{p,i} \frac{dT_{p,i}}{dt} =$$
$$\sum_{j=1}^{\gamma} Q_{Cond,p-p,ij} + Q_{Cond.p-f-p} + Q_{Conv.} \tag{21}$$

Then, the particle temperature $T_{p,i}$, for instance $(t+\Delta t)$ becomes:

$$T_{p,i}^{t+\Delta t} = T_{p,i}^{t} + \frac{\Delta t}{m_{p,i} C_{p,i}}$$

$$\left(\sum_{j=1}^{\gamma} Q_{Cond,p-p,ij} + Q_{Cond.p-f-p} + Q_{Conv.}\right) \quad (22)$$

The active interplay between the fluid and particles in CFD-DEM simulations allows for precise forecasting of localized temperature distributions and heat transfer coefficients within the system.

4. Combined CFD-DEM with thermal model

The research utilized a systematic CFD-DEM simulation methodology to examine how particle and column sizes affect local heat transfer within liquid-solid fluidized beds. The study analyzed two column diameters (51 mm and 96 mm) alongside three particle diameters (2, 3, and 5 mm) while maintaining a constant inlet wall temperature of 90°C and four different fluid entrance velocities (ranging from 0.08 to 0.20 m/s). Figure 1 illustrates the numerical methodology used for the CFD-DEM analysis of the heat transfer process within the liquid-solid packed and fluidized beds. The numerical methodology starts with the pre-processing steps, which include geometry definition, mesh generation, and thermo-physical property definition for the fluid and the solid particles. Next, the CFD-DEM numerical model for the fluid and the solid particles is used to obtain the temperature distribution within the fluidized bed, which is solved with the thermal model for the fluid-particle convection and the contact conduction among the solid particles. The temperature distribution within the fluidized bed is used to obtain the rate of heat transfer and the corresponding performance parameters. In this research, the equations that regulate fluid dynamics and thermal transfer were examined through the CFD framework, whereas the movement and interactions of discrete particles were represented using the DEM component. This combination of solvers enabled a thorough representation of momentum transfer and heat transfer between the fluid and the particles. This methodology yielded dependable data that could be employed to enhance heat transfer in fluidized systems.

5. Results and Discussion

The present work explored the influence of particle size and column inner diameter on heat transfer performance in liquid-solid fluidized beds through a CFD-DEM coupled method. The findings reveal complex interactions between hydrodynamics and thermal transport with strong dependence on geometrical and particle-scale parameters.

5.1 Hydrodynamics validation of the coupling CFD-DEM

Simulations performed on spherical particles (d_p= 2.0 mm) have been simulated. The numerical results come from the column with a diameter of 96 mm and a height of 1 m, in which an ascending fluid (water) passes through spherical particles made up of glass beads, resting bed height initially at (H_o=100 mm), over a range of inlet water velocities in the range (0.02- 0.14 m/s) through the bed. Values of the parameters are shown in Table 1. The numerical results have been plotted in Figure 2 against experimental findings from literature [62].

The Comparison between the numerical and experimental findings is done in terms of maximum expansion ratio (H/H_o) with the velocity ratio (v_f/V_{mf}), where V_{mf} is the minimum fluidization velocity calculated from Wen & Yu correlation [66]. The bed is relatively compact for lower velocities, while the particles are suspended for higher velocities, pointing toward the formation of complete fluidization. The numerical results based on Syamlal and O'Brien's drag law exhibit a robust correlation with the experimental results in the region of (0-0.14 m/s). Figure 2 shows the numerical results in terms of the maximum bed expansion ratio (H/H_o) versus the velocity ratio (v_f / V_{mf}) in comparison with the experimental results. As shown in the results, the numerical results by the CFD-DEM model agree well with the experimental results, with an average deviation of about 5-7% and an error of less than 10%. The difference between the numerical results and the experimental results can be explained by the fact that in numerical simulation, the properties are ideal, like the sphericity of the particles, and complicated effects such as particle shape irregularity and wall roughness were all excluded, which may affect the hydrodynamics of real systems.

5.2 Application of a coupled CFD-DEM with a thermal model in the fluidization process

To model heat transfer effects in liquid-solid fluidized beds, a column that contains a bed of spherical aluminum balls with various particle diameters (2, 3, and 5 mm) and have initial temperature of 20 °C (i.e, 293.15 K). The initial bed height is 100 mm, the column inner diameters (D = 51 mm, and D = 96 mm), column height is 720 mm, and crossed by a rising liquid (water) for a range of fluid velocities (v_f = 0.08-0.20 m/s). The parameter values for aluminum and water are given in Table 2.

The number of particles (N_p) according to particle size and column diameter was as following; for D= 51 mm ($N_{p,2\ mm}$ =1840, $N_{p,3\ mm}$ =578, and $N_{p,5\ mm}$ =242), and for D= 96 mm ($N_{p,2\ mm}$ =2400, $N_{p,3\ mm}$ =1088, and $N_{p,5\ mm}$ =440).

Uniform velocity inlet for liquid (water) at ambient

temperature 20 ºC (i.e, 293.15 K). The inlet wall was maintained at a constant temperature (isothermal), T_w = 90 ºC (i.e, 363.15 K), and adiabatic for sidewalls, all other walls, and the outlet is open, as well; it is presumed that the temperature is evenly distributed throughout each particle. The meshing are unstructured tetrahedral elements with fine resolution and a time step of 10^{-4} seconds; the mesh properties are depicted in Table 2, and the mesh independence and convergence criteria have been checked in previous research [62].

5.3 Effect of geometrical parameters on bed height (expansion)

In this section, it will examine how particle size and the inner diameter of the column influence hydrodynamic, particle-fluid interaction, including bed height (expansion), which directly affects heat transfer within the fluidized bed. The bed expansion in liquid-solid fluidized beds is governed by the balance between the drag force due to the upward flow of liquid and the total weight of the particles, including the effect of buoyancy. The bed expansion affects heat transfer coefficients by changing solid holdup, contact area, and mixing of particles. Higher bed expansion is associated with: *i*) augmented convective heat transfer through heightened particle motion, *ii*) Reduction of conductive pathways due to higher voidage, particularly in narrow columns with small particles. Geometrical influences on bed height have a direct effect on heat transfer processes presented later. Figure 3 plots illustrate bed height as a function of time for different particle sizes (d_p = 2, 3, 5 mm) and column diameters (51 mm, 96 mm). Liquid-solid fluidized bed expansion is due to the equilibrium of the upward drag force and the weight of the particles. For $v_f > V_{mf}$, the suspension of particles becomes higher, which causes higher bed height and voidage. For the narrow column, where the diameter, D= 51 mm, the behavior of the particles with a diameter, d_p= 2 mm, is depicted in Figure 3(a). It is evident that the bed height expands quickly as the flow of the liquid is initiated and that the height of the bed is higher at steady expansion with the increase in the fluid velocity (v_f), from 0.08 to 0.20 m/s. The distinct variation of the curves at different velocities proves that the expansion of the bed is very sensitive to the variation of the velocity of the fluid. The behavior of the particles with a diameter of 2 mm could be explained by the fact that the particles have a large surface area to volume ratio and low inertia, and therefore, the drag force acting on the particles is enhanced with the increase in the velocity of the fluid. Moreover, Figure 3 (c) presents (d_p = 3 mm), monotonic ordering with fluid velocity is the same, but absolute expansion at a specified fluid velocity (v_f) is less than for 2 mm (larger particles give a bigger V_{mf}, smaller v_f / V_{mf} at the same v_f). Small oscillations around the plateau are more evident, in accordance with the increased particle inertia. While Figure 3 (e) presents (d_p = 5 mm), where the bed height (expansion) is lowest at a given fluid velocity and the velocity curve separation is decreased, i.e., you require a greater increment of v_f to achieve the same ΔH. For a D = 51 mm column, the (D/d_p) ratio is near ~10, so wall effects dampen expansion and can foster macro-voids or non-uniform solid holdup.

In evaluating the performance of a wide column measuring 96 mm in diameter, as depicted in Figure 3, it observes various trends related to particle diameter (d_p) and voidage fraction are observed. Figure 3 (b) presents (d_p = 2 mm), the expanded bed height in this configuration is notably higher compared to that observed in a 51 mm column. Whereas Figure 3 (d) presents (d_p = 3 mm), the expansion noted here falls within the range established by the previous two configurations, Figure 3 (a) and (e). Despite this, it remains larger than the expansion recorded for the 51 mm column across all v_f levels. The temporal oscillations around the plateau are relatively moderate, indicating reduced wall friction and a more consistent hydrodynamic flow in the larger diameter column. Figure 3 (f) depicts (d_p = 5 mm), the bed height is less than the two other sizes due to the weight of the particles. Although this configuration utilizes the largest particles, the 96 mm column still demonstrates a significantly greater degree of expansion compared to the 51 mm column at equivalent fluid velocity values. Furthermore, the separation among the four fluid velocity curves is more pronounced, showcasing the influence of each of the inlet flow rate, particle buoyancy, and the increase in the sensitivity of voidage to fluid velocity as wall effects are effectively minimized. Consequently, in the small-diameter column (51 mm), particle size expansion differences are more extreme at low velocities, which reflects intense geometry-particle coupling. While in the wide diameter column (96 mm), expansion curves converge rapidly, with decreased wall effects. Overall, the results emphasize the benefits of using a wide column, especially regarding better solids redistribution and diminished confinement effects, which contribute to enhanced performance metrics across different particle sizes. While narrower columns heighten hydrodynamic interactions between the walls and particles, potentially stabilizing the suspension and promoting increased voidage near the walls.

5.4 Validation of the coupling CFD-DEM combined with thermal model

The combined CFD-DEM with the thermal model has been validated by comparing numerical predictions with the well-established experimental results of Gunn [60], using particle Nusselt number (Nu_p) and

particle Reynolds number (Re_p) as the main indicators of performance. The physical properties of the system are listed in Table 4. The simulation setup also replicated the thermal conditions: the bed of particles was initially at 293.15 K, with hot fluid (Therminol 66) at 473.15 K introduced from the bottom at a superficial velocity of 0.005 m/s to make sure the thermal gradients represented what was measured originally.

Figure 4 shows a comparison of numerical predictions with experimental data in terms of particle Nusselt number, Nu_p, as a function of particle Reynolds number, Rep. It can be observed that numerical results follow the increasing trend of experimental results. Therefore, it can be concluded that the CFD-DEM model captures the dominant particle-fluid heat transfer mechanisms in the system. With increasing values of Re_p, Nu_p also increases, showing that convective heat transfer between particles and fluid becomes more dominant. At lower values of Re_p, conduction plays a dominant role in heat transfer between particles and fluid, as the boundary layer between particles and fluid becomes thick. With increasing values of Re_p, the relative velocity between particles and fluid increases, resulting in a thinner boundary layer between them, thus increasing the rate of heat transfer. The reliability of the model has been quantified in terms of the percentage deviation between the predicted and experimental values of the particle Nusselt number presented in Figure 4. It has been observed that the results obtained from the CFD-DEM simulation have a good agreement with the experimental data, and the average deviation is within the range of 6-8%, while the maximum error is less than 10%. The minor discrepancies with the results obtained by Gunn are due to local differences in the parking structure and contact conductive heating, each of which can affect convective behavior. The overall validation indicates that the CFD-DEM model provides a valid simulation of particle heating.

5.5 Influence of geometric parameters on Re-Nu relationship

Having a mathematical correlation between hydrodynamic conditions and convective heat transfer enhances the estimation of the convective heat transfer coefficient, reducing reliance on complex experimental data. In the CFD-DEM framework, these correlations improve the predictive accuracy of thermal modeling at the particle level and offer reliable validation against empirical data. This method also allows adaptation across different particle sizes, column diameters, and superficial velocities. Throughout the six datasets in Figure 5 (a-f), particle Nusselt number (Nu_p) rises with particle Reynolds number (Re_p), showing a gradual curvature at lower Re_p values and tending towards an almost linear trend for higher Re_p values. The symbol sets for the four superficial liquid velocities (v_f = 0.08-0.20 m/s) collapse onto a single master curve when plotted against Re_p, thus verifying that Re_p is the leading governing similarity parameter for particle-scale convective heat transfer in the experiments performed.

The investigation of how particle size influences the Re-Nu relationship while maintaining a constant column diameter is outlined as follows; For column diameter D = 51 mm: As the particle diameter (d_p) increases from 2 mm to 3 mm and then to 5 mm Figure 5 (a, c, e), the spectrum of the open particle Reynolds number (Re_p) interval shifts toward the right, (approximately from 0-380 to 0-750, and then to 0-1150). Meanwhile, the particle Nusselt number (Nu_p) remains consistent within the same range (around 0-20). This observation indicates that the predominant effect of larger particles is to elevate Re_p, rather than altering the functional relationship between Nu-Re. At a constant Reynolds number, particle Nusselt number does not show a significant systematic variation with changes in particle diameter. While, for the column diameter of D = 96 mm, the observed trend persists, where particle diameter (d_p = 2 and 3 mm) spans (approximately 0-400 and roughly 0-800) in Re_p (Figure 5 (b, d)), whereas d_p = 5 mm achieves values up to about 1280 (Figure 5 (f)), with Nu_p consistently limited to around 20. A merging of multi-velocity data into singular curves is also noted, suggesting that heat transfer is regulated at the particle level through Re_p.

On the other hand, the influence of column diameter on the consistency of particle size (d_p = 2, 3, 5 mm) is examined. For particle diameter (d_p = 2 mm), Figure 5 (a), (b), the columns of D = 51 mm and D = 96 mm feature very similar Nu_p-Re_p envelopes (Nu_p to $\lesssim$20 over Re_p $\lesssim$500). Whatever diameter-wise offset, if any, is present is minor relative to the overall trend and within the visual scatter of the collapsed data sets. Figure 5 (c, d) depicts the particle diameter (d_p = 3 mm), both diameters reveal similar Nu-Re profiles for Re_p values around or below 800, indicating little to no systematic difference between D = 51 mm and D = 96 mm at the same Re_p levels The Figure 5 (e), (f) illustrates the particle diameter (d_p = 5 mm): The larger column attains a higher Reynolds number ceiling (~1300 compared to ~1200), indicating a wider operating range at elevated flow rates; however, the Nu-Re scaling in the overlapping range remains unchanged. Finally, Figure 5 revealed the phenomena of curve agglomeration with the increase of particle diameter (d_p = 3 and 5 mm) and for both column diameters. This can be justified based on the fact that particles take time to reach a state of complete fluidization, and then the particles move up and down within a certain range inside the column.

5.6 Thermal simulation of liquid-solid fluidized beds

The transfer of heat in liquid-solid fluidized beds involves conduction and convection. Conduction occurs through direct thermal energy transfer in solids and fluids, particularly in densely packed areas where inter-particle collisions happen. In CFD-DEM, conductive heat transfer is represented by thermal resistance at contacts. The lumped-capacitance assumption (Biot number $\ll 0.1$), for the three particle sizes (d_p = 2, 3, 5 mm), is justified for $h_{p,f}$=100-1000 [W/(m^2.K)] (Bi_{2mm}=0.0021, Bi_{3mm}=0.0031, and Bi_{5mm}=0.0052). Figure 5 illustrates the comparative analysis of heat conduction at constant inlet temperature (T_w= 90 °C) for two column diameters (D = 51 mm, 96 mm) and three particle sizes (d_p = 2, 3, 5 mm). Heat conduction is observed to increase with both particle size and low inlet fluid velocity (0.08 m/s) in both column types. The wider column (96 mm) exhibits more uniform time traces; however, the overall magnitudes at a constant particle diameter are comparable between the two columns. This indicates that conduction is primarily influenced by the physics of local contact, with geometry playing a secondary role through hydrodynamic structuring and spatial averaging.

Figure 6 is specified range is sufficient to convey the extent of conduction for every case, the effects of geometrical parameters (particle diameter, and column diameter) on conduction energy transmit are detailed as; For column diameter fixed, particle size effect; for narrow column D = 51 mm, systematic expansion of the plotted ranges with particle diameter (d_p = 2 mm) about 0.22 W (Figure 6 (a)), the 3 mm panel about 1.5 W (Figure 6 (c)), and the 5 mm about 1.9 W (Figure 6 (e)) which is more evidence that larger particles yield a greater instantaneous conductive burst in this column. While for wide column D = 96 mm: as particle diameter increases, it can see the same monotonic rise in all envelopes from about 0.31 W (2 mm) to 0.6 W (3 mm) and 1.4 W (5 mm) as depicted in Figure 6 (b), (d), (f). The interpretation for conduction energy magnitude increases with particle diameter (d_p) is that in a contact-based solid-solid conduction model (such as CFD-DEM), bigger particles make contacts with bigger Hertzian contact areas and greater per-contact thermal conductance.

The results show that particle size determines the main effect of conduction in liquid-solid fluidized beds (larger particles present higher instantaneous conduction), where the conduction heat transfer for small column (D= 51 mm and v_f=0.08 m/s), increased by approximately 88% when particle diameter increased from 2 mm to 5 mm and increased by approximately 79% for large column (D= 96 mm). This difference in percentage between the two columns is caused by the particles' expansion for d_p= 5 mm in the small column being less than in the large column, as depicted in Figure3 (e and f), which gives the particles more time to heat transfer by conduction. Then, fixed particle size, effect of column diameter; at the same particle diameter, as with distance reduction, amplitude envelopes between D=51 mm and D=96 mm (with matching y-axis limits case-by-case) are comparable yet again, suggesting no major alteration to peak conductive exchange exclusively through column widening as shown in Figure 6 (a, b); (c, d); (e, f). The indicator of conductive exchange is traces that exhibit both positive and negative values, illustrating bidirectional heat transfer at specific interfaces, such as from a cooling particle to a hotter neighbor or wall, and conversely from a heated particle to a cooler environment (see Figure 6 (c, e)). At the same time, while trends are nearing zero, there is still volatility as heated particles continue to combine before they ultimately separate.

The results indicate that the temporal characteristics of the signal exhibit variations, as evidenced by the shape of the multiple curve traces (Figure 6); however, visual comparison shows that wider columns typically have higher core-dominated solids circulation and a smaller wall-area to bed-volume ratio as illustrated in Figure 5, which tends to transfer conduction from particle to particle contacts toward less frequent, shorter events rather than extended periods of stable contact. Consequently, the particles are in closer contact, leading to a higher level of conduction energy in the (51 mm) column when compared to the 96 mm column, where in the large particle sizes (d_p = 3 and 5 mm), the contact area between the particles is larger according to eq. 16 will lead to an increase in the heat transfer by conduction (see Figure 6 (c), (e)).

The predominant heat transfer mechanism in liquid-solid fluidized beds, in which solid particles are supported and dragged by liquid flow, is convection. In such systems, convective transport occurs as a result of the relative motion between the fluid and the particles. Figure 7 (a-f) shows the instantaneous convective heat energy transfer for six cases by CFD-DEM, which was obtained by intersecting two inner column diameters (D = 51 and 96 mm) with three different particle diameters (d_p = 2, 3, and 5 mm). The inlet wall temperature was set at 90 °C, while the inlet liquid velocity (v_f) was set at (0.08-0.20 m/s). The effects of geometrical parameters (particle diameter, and column diameter) on convection energy transmit are detailed as; for fixed column diameter, particle size effect; the convection heat transfer in narrow column (51 mm), for the smaller particle size (2 mm)

is depicted in (Figure 7 (a)), where the convection heat transfer rates reached relatively low values (up to ~500 W).

At low velocity (0.08 m/s), the system shows slow growth of heat transfer because of the limited fluid-particle mixing. With a further increase in velocity to 0.20 m/s, the enhanced fluid circulation in stronger circulation flow results in an increased disruption of the boundary layer, which causes an additional strong increase in convective flux. The increase in particle size to 3 mm (Figure 7 (c)) almost doubles the maximum heat transfer compared to a particle diameter of 2 mm, reaching 1000 W, due to better bed porosity as well as more effective fluid turbulence around larger particles, resulting in higher mixing and a higher interfacial area for convective exchange. However, the cycle becomes more evident as time progresses, which means that more violent, unsteady flow patterns are produced.

At 5 mm (Figure 7 (e)), convection cooling is enhanced, reaching 1300 W. Further increased agglomerates lead to increased wakes and enhance the global macro-scale mixing (even with higher velocities (0.16-0.20 m/s)). The longer time axis (to 20 s) also shows sustained convective transfer, with large amplitude oscillations arising from cycles of periodic bed expansion and collapse. The convection heat transfer for a wide column (96 mm), for 2 mm diameter particles (Figure 7 (b)), convective heat transfer is close to 2000 W in wide-bore columns compared to ~500 W in a narrow column. The larger cross-section reduces the wall effect; expansion and particle circulation are smoother, which can improve the effective heat transfer coefficient. The scaling was especially pronounced at velocities above 0.16 m/s. The convective heat transfer is further increased to almost 1650 W by using 3 mm particles (Figure 7 (d)). In comparison to the 51 mm column, the wider column, 96 mm, brings about more intense particle-liquid convection loops as well as a more even distribution of eddies.

The transient data present a sharp peak at the beginning and almost steady oscillations after a short time, indicating that a dynamic balance is established very quickly between the suspensions and settling of the particles. While maximum convection values are achieved with 5 mm particles in the 96 mm column (Figure 7 (f)), up to 2000 W at maximum liquid velocity (v_f = 0.20 m/s). The findings in Figure 7 show that particle size determines the main effect of convection in liquid-solid fluidized beds, where the convection heat transfer for a small column (D= 51 mm and v_f=0.08 m/s) decreased by approximately 14% when particle diameter increased from 2 mm to 5 mm, and decreased by approximately 45% for a large column. At the same particle size and flow conditions, the 96 mm column always reaches greater peak convective heat energy than the 51 mm column. This is due to the greater cross-sectional area and greater bed voidage at similar superficial velocities, which allows for enhanced liquid-solid contact and greater interfacial surface area for heat transfer. This is the result of weaker wall confinement and increased bulk flow in the larger geometry. While the effect of inlet fluid velocity in all cases, increasing the superficial velocity from 0.08 to 0.20 m/s significantly enhances convective heat transfer in the column. This higher velocity reduces both hydrodynamic and thermal boundary-layer thickness around the particles and the wall, thereby reducing the interfacial thermal resistance and enhancing the local heat-transfer coefficient. Also, with an increase in the particle Reynolds number, this intensifies particle-fluid convective heat transfer, often modeled as:

$$(h_{p,f} \propto \mathrm{Re}_p^{0.6}\, \mathrm{Pr}^{0.33}).$$

Stronger turbulence and thermal mixing enhance the effective thermal diffusivity of the fluid and accelerate the transport of hot and cold fluid parcels. The intensified flow strengthens the relative motion between the fluid and the particles, enhancing particle-fluid heat exchange. Accordingly, the combined effects of boundary-layer thinning, enhanced turbulence, and increased solid-fluid interaction result in substantial growth of convective heat transfer with increasing superficial velocity. The convection findings are enhancing the Nusselt number of the particles (Nu_p), which was obtained from the local and averaged convective heat transfer coefficients, which were determined from the CFD-DEM simulations. These values are related to the increment of superficial liquid velocity. When this increases from 0.08 up to 0.20 m/s, the Nusselt number goes up regularly due to a stronger mixing of the particles with the fluid and good renewal of the heat-transfer surface area.

In addition, relate this behavior explicitly to the transition between flow regimes. For low velocities, close to 0.08 m/s, the bed is in a state of a packed or weakly expanded system, where the heat transfer mechanism is dominated by conduction through fixed or slowly moving particles. When the velocity approaches and exceeds the minimum fluidization point, the system enters the fully fluidized regime, characterized by large particle agitation and liquid–solid slip. This leads to a marked increase in the convection-driven Nusselt number.

These findings are further correlated, for the first time, with the change in hydrodynamic regime. Below the velocities corresponding to incipient fluidization, the bed stays either fully packed or weakly expanded, with the dominant contribution of heat transfer via conduction through nearly stationary particles. When the velocity reaches and exceeds that corresponding to the minimum fluidization point, the bed is fully

fluidized, resulting in higher mobility of the particles, higher slip velocities, and hence stronger convective transport. These regime-dependent phenomena are now incorporated into the interpretation of Figure 7. The results confirm that convection is predominant at high fluidization intensities and conduction is more prevalent at low velocities.

Snapshots of the heating process in a liquid-solid fluidized bed are depicted in Figs 8 and 9, through a series of images for two column diameters (D = 51 mm and 96 mm) and three particle sizes (d_p = 2, 3, and 5 mm). Figs 8 and 9 phase diagrams and temperature distribution diagrams, in which the fluid (water) temperature is within a range between 293.15 K and 363.15 K. The color regions demonstrate the distribution of temperature in the column (blue for the cold fluid region and red for the hot fluid region). The transient temperature distribution serves to demonstrate how particle size, column diameter, and liquid mixing influence the thermal dynamics of the bed.

For the narrower column (D = 51 mm) with d_p = 2 mm (Figs 8 (a)), at the outset (t = 0.0-0.5 s), initially, the bed remains still, with all particles at a uniform cool temperature (initial bed temperature 293.15 K) as indicated by the blue region. Fluidization begins immediately due to the relatively high inlet velocity, resulting in a uniformly fluidized bed. The rapid heat penetration from the heated wall is attributed to the smaller particle size and the larger surface area-to-volume ratio. In the transitional phase (t = 1.0 - 3.0 s), the bed expands rapidly, creating a uniform region characterized by extensive solid mixing. The homogeneous mixing facilitates a more even distribution of heat throughout the bed height. The final stage (t = 5.0 - 10.0 s), where the bed approaches an isothermal state, is evidenced by the dominant red hue along its height.

The Figs 8 (b) presents the heating with d_p = 3 mm (t = 0.0-0.5 s), in which the bed starts at rest, with blue regions indicating lower temperatures. Fluidization is slightly delayed compared to the 2 mm case due to the increased inertia of the larger particles. Then the intermediate stage (t = 1.0-3.0 s), the bed expands. The heating zone progresses more slowly than with 2 mm particles due to the smaller surface area and reduced mixing efficiency. Final Stage (t = 5.0-10.0 s), the red region covers a significant portion of the bed, although it is less consistent compared to the 2 mm situation.

In Figs 8 (c), the largest particles (d_p = 5 mm) exhibit significantly slower heating behavior. Initially (t ≤ 0.5 s), a very thin thermal boundary layer develops near the side wall, while the main fluid region retains its low initial temperature. Between (t = 1.0-3.0 s), heating primarily ascends from the bottom to the top; however, due to the smaller surface area of the particles and their greater inertia, mixing intensity diminishes. By t = 5.0-10.0 s, noticeable inhomogeneities remain in the core, indicating that conduction is the primary mode of thermal transport in this arrangement. The Figs 8at the outset (t = 0.0-0.5 s) illustrates the situation of particle vertical alignment affected by the inner surfaces of a narrow column and the dimensions of the particles, particularly focusing on sizes (d_p = 3 and 5 mm) as depicted in Figs 8 (b), (c).

For the larger column (D = 96 mm; d_p = 2 mm), the initial heating phase resembles that of the smaller column. As illustrated in Figure 9 (a) (for t = 0.0 s), the color scheme indicates temperature distribution, where blue corresponds to low-temperature regions (initial conditions), and red signifies higher-temperature areas, reflecting the evolution of heating and thermal penetration throughout the bed.

Utilizing information from Figures, t = 0.25 s: localized heating initiates at the base and near the walls, leading to the development of the thermal boundary layer due to direct conductive and convective heat transfer from the wall to adjacent particles and liquid. The bed begins to expand as the superficial velocity exceeds the fluidization threshold ($v_f > V_{mf}$). Then, for t = 0.5 s, the heated area (red zone) rises, and enhanced convection distributes heat from the bed's bottom to the upper sections. At (t = 1.0 s), fluidization strengthens, with the thermal front penetrating further into the bed. The mixed region displays robust convective mixing and particle movement, resulting in a more uniform radial temperature profile than observed in initial snapshots. By t = 3.0 s, both axial and radial mixing are enhanced, reducing the thermal gradient; however, the restoration of thermal uniformity is slowed, with vestiges of cooler fluid persisting within the bulk. Quasi-steady state conditions result from the combined effects of rapid charge exchange reactions. At (t = 5.0 s), the bed approaches a steady fluidization state, displaying a red-blue pattern throughout the bed's height, indicating improved uniformity. Heating fully developed at (t = 10 s), where the process reaches a state of near-thermal equilibrium, with temperature uniformity across the fluidizing bed. Effective mixing of particles and fluid ensures that both conduction (particle-particle and particle-wall) and convection (fluid-particle) contribute to rapid heating homogenization.

Figure 9 (b) presents particle diameter (d_p = 3 mm) for the preliminary stage (t = 0.0-0.5 s): the initiation of fluidization is slightly slower compared to the 2 mm bed case, attributed to the increased influence of particle inertia. The heated wall transitions to the red front in a more gradual manner. Then, intermediate stage (t = 1.0-3.0 s): thermal layers with stratified profiles dominate the flow, and although circulation

zones promote homogenization, their turnover times are insufficient for rapid heat distribution. By t = 3.0 s, significant but uneven heating is noted, with cooler regions (depicted in blue) present in the upper layers, where circulation is less vigorous than in the 2 mm bed situation.

At last, for quasi-steady state ($5.0 \leq t \leq 10.0$ s): at t = 5.0 s, the bed is nearing a quasi-steady thermal condition, where enhanced turbulence and particle movement facilitate a uniform temperature distribution throughout the depth of the bed. The combined effects of intensified liquid-solid interactions, increased turbulence, and stabilized fluidization contribute to the swift homogenization of the thermal field. By t = 10.0 s, the bed is approaching a thermal steady state, indicated by a red color field that signifies nearly complete heating of both the liquid and the particles. Minor gradients remain near the free surface, primarily due to the lower concentration of particles and reduced mixing intensity in this upper layer.

The largest particles (d_p = 5 mm) within the D = 96 mm column demonstrate the most significant lag in heating, as illustrated in Figure 9 (c). At t = 0.0 s, the system is in a packed bed configuration, with particles settled at the bottom of the column and the liquid phase uniformly cold. The column shows no evidence of heating penetration, resulting in a flat temperature profile (indicated by the blue zone). During the initial phase of fluidization (from t = 0.25-0.5 s), the movement of particles begins as the fluid overcomes inertia, lifting and rearranging the particles, which decreases bed porosity. At this stage, heat transfer is predominantly governed by wall-to-particle conduction, as evidenced by the development of a red boundary layer along the column's heated wall. For larger particles, heat penetration radially is constrained due to their lower surface area-to-volume ratio compared to that of finer particles. The intermediate fluidization at (t = 1.0 s), the bed is fluidized, with particles circulating more extensively and bubble formation within the bed. The temperature field reveals significant penetration of heated liquid towards the center of the bed; however, the bulk zone shows cooler areas compared to the core, indicating an inhomogeneous thermal distribution during the initial mixing phase. By (t = 3.0 s), transitional heating, enhanced interactions between fluid and particles, as well as among the particles themselves, lead to increased convective mixing.

Quasi-steady heating at (t = 5.0 s), the system reaches a quasi-steady heating state, and the combined effects of convective circulation and conduction between particles and walls facilitate a quicker approach to thermal equilibrium. Nonetheless, small temperature gradients persist, influenced by the size effect on the rate of heat penetration. The heating is reached fully developed (t = 10.0 s), and the process reaches a state of near-thermal equilibrium, with temperature uniformity across the fluidizing bed. Effective mixing of particles and fluid ensures that both conduction (particle-particle and particle-wall) and convection (fluid-particle) contribute to rapid heating homogenization.

In comparison, the particle size (d_p = 5 mm) case shows slower thermal uniformity relative to smaller particle sizes (2 and 3 mm), consistent with their lower surface areas and smaller Nusselt numbers. Figures. 8 and 9 illustrate time-averaged bed temperature as a function of time, computed from the CFD-DEM temperature fields. This provides a straightforward measure of the overall heating rate within the column and enables easier comparison between cases. Results are presented showing that wider columns have a slightly slower average temperature rise because of their larger cross-sectional area and reduced local mixing, while beds of smaller particles (d_p= 2 mm) heat faster due to their higher surface area to volume ratio and more intense particle/fluid contact.

The spatial temperature variance, included herein and serving as an index of thermal uniformity, provides a quantitative measure of the amount of temperature stratification present across the bed. The results indicate that the temperature variance drops more quickly in the narrow column, therefore homogenizing faster, while in the wide column, the bed takes longer to become uniform. In the same vein, beds containing (d_p= 2 mm) particles reach a lower variance sooner than those with (d_p= 5 mm) particles because of the higher efficiency in convective heat transfer.

6. Conclusions

The current study systematically explored the influence of particle size and column diameter on hydrodynamics and heat transfer in liquid-solid fluidized beds across a series of inlet liquid velocities (0.08-0.20 m/s). The CFD-DEM simulations reveal that liquid-solid fluidized bed heat transfer is strongly coupled by particle size, column diameter, and liquid velocity. Convection was found to be the dominating mechanism when the bed had already passed from a packed condition to a fully fluidized state. Thermal transport is controlled by conduction at low velocities ≤0.10 m/s due to poor mobility of the particles. Higher velocities increase the particle-fluid interactions,

leading to higher convective heat transfer. According to the numerical simulation results, the following conclusions are presented:

1. Quantitatively, smaller particles (2 mm) create the best thermal performance and result in a big increase in the effective heat transfer coefficient compared to 5 mm particles owing to increased surface area and, therefore, improved temperature uniformity. Larger columns (96 mm) also assist with better thermal behavior by providing notably greater bed expansion, enhanced solids mixing, and more uniform radial temperature fields compared to the 51 mm column.
2. The optimum range of operation was found to be within a velocity range of 0.12 to 0.16 m/s, where particle circulation, bubble activity, and convective transport are at a balanced regime. This range gives not only the most efficient heat transfer performance with the combination of a 96 mm column with particles diameter 2 and 3 mm, but also the most stable hydrodynamics. Large particle diameter (5 mm) and small diameter column (51 mm) systems present poor fluidization quality and reduced heat transfer, mainly in the low-velocity range.
3. Overall, the current research has revealed that column diameter and particle size are the significant design factors that can directly influence the hydrodynamic and thermal transfer mechanisms in liquid-solid fluidized beds. The application of the CFD-DEM method has given a clear view of the relationship between the movement of the particles and the thermal transfer mechanisms, and the results are considered useful for the design of fluidized bed systems for use in slurry reactors, catalytic cracking units, and thermal treatment units.

Despite the detailed CFD-DEM analysis undertaken within the present study, a few limitations should be pointed out. These simulations are for ideally spherical particles with uniform thermal properties, and complicated effects such as particle shape irregularity and wall roughness were all excluded, which may affect the hydrodynamics and heat transfer of real systems.

It is necessary to carry out further research to study the effect of geometrical parameters on heat transfer in fluid-solid fluidized beds to improve design and optimize thermal performance in fluidized beds. It has been found that numerical analysis would be useful to understand the effect of changes in column diameter and other geometrical properties using CFD-DEM analysis. Such knowledge would be useful to scale up fluidized beds to improve efficiency in fluidized beds. For further research, the current model needs to be developed for use with non-spherical particles, temperature-dependent properties, and realistic boundary conditions so that the application of the CFD-DEM method can be more realistic for the design of thermal fluidized bed systems.

References

[1] Kunii, D., Levenspiel, O., *Fluidization Engineering*. 1991, 2nd ed., Butterworth-Heinemann.

[2] Osnes, A. N., Vartdal, M., *Performance of drag* force *models for shock-accelerated flow in dense particle suspensions*. International. Journal Multiphase Flow, 2021. **137**: 103563. https://doi.org/10.1016/j.ijmultiphaseflow.2021.103563.

[3] *Yang*, W. C., *Handbook of Fluidization and Fluid-Particle Systems*. 2003, CRC Press, Taylor & Francis Group.

[4] Bi, H.T., Grace, J.R., Zhu, J.X., *Wall effects in fluidized beds and risers*. Powder Technology, 2000. **113**: p.1-10.

[5] Vahid, T., Alberto, P., Shankar, S., *Particle-resolved simulation of freely evolving particle suspensions: Flow physics and modeling*. International Journal of Multiphase Flow, 2020. **135**: 103533. https://doi.org/10.1016/j.ijmultiphaseflow.2020.103533

[6] *Deen*, N.G., Annaland, M.V.S., van der Hoef, M.A., Kuipers, J.A.M., *Review of discrete particle modeling of fluidized beds*. Chemical Engineering Science, 2007. **62**: p. 28-44. https://doi.org/10.1016/j.ces.2006.08.014

[7] Rajashekhar, P., Roy, S., *CFD-DEM modelling of hydrodynamics and heat transfer in gas-solid fluidized beds*. International Journal of Heat Mass Transfer, 2013. **116**: p. 377-392. DOI: 10.1016/j.ijheatmasstransfer.2017.09.015.

[8] Xue, J., Xie, L., Shao, Y., Zhong, W. *CFD*-DEM *study of the effects of solid properties and aeration conditions on heat transfer in fluidized bed.* Advanced Powder Technology, 2020. **31** (9): p.3974-3992. https://doi.org/10.1016/j.apt.2020.08.002

[9] Deng, Z., Wang, S., He, Y., Liu, H., Xu, D., *CFD-DEM simulation of hydrodynamics and heat transfer in gas-solid fluidized beds with different particle sizes*. Powder Technology, 2020. **366**: p. 35-46.

[10] Olazar, M., Arandes, J. M., Bilbao, J., Castaño, P., *Heat transfer in fluidized beds with small inner*

diameter. Chemical Engineering Science, 2000. **55**: p. 927-936.

[11] Ritacco, H.A., Montane, J.M., Miralles, J. A., *Heat transfer in liquid-solid fluidized beds with different particle sizes*. Chemical Engineering Journal, *2013*. 215-216: p. 696-704.

[12] Peng, Z., Duan, C., Wang, Z., *Influence of particle size on the fluidization and heat transfer characteristics in liquid-solid systems*. Powder Technology, 2013. **332**: p. 262-270.

[13] Li, T., Mason, J., *Radial voidage profiles in packed beds: Effect of column diameter and particle size*. Chemical Engineering Science, 2010. **65**: p. 409-417.

[14] Fan, L.S., Zhu, C., *Principles of Gas-Solid Flows*, 1998. Cambridge University Press.

[15] Gidaspow, D., *Multiphase Flow and Fluidization*, 1994. Academic Press, New York.

[16] Li, T., Mason, J., *Wall effects in small diameter liquid-solid fluidized beds*. Chemical Engineering Science, 2006.

[17] Rowe, P.N., Nienow, A.W., *Particle mixing and segregation in gas fluidized beds: A review*. Powder Technology, 1976. **15**: p. 141-147, 1976.

[18] Akhil, R., Jennifer, C., Bruno, C. H., Carl, R.W., *The Effect of Column Diameter and Bed Height on Minimum Fluidization Velocity*. Aiche Journal, 2010. https://doi.org/10.1002/aic.12161

[19] David, C. A., Liang-Shih, F., *Experimental methods and correlation of solid-liquid mass transfer in fluidized beds*. Chemical Engineering Science, 2010. **45** (4): p. 965-975. https://doi.org/10.1016/0009-2509(90)85019-A

[20] *Chen*, Y., et al., "Influence of wall confinement on hydrodynamics and heat transfer *in* fluidized beds. Powder Technology, 2015. **15**: p.141-147.

[21] *Tsuji*, Y., *Tanaka*, T., Ishida, T., *Lagrangian numerical simulation of plug flow of cohesionless particles in a horizontal pipe*. Powder Technology, 1992. **71** (3): p. 239-250. https://doi.org/10.1016/0032-5910(92)88030-L.

[22] Lu, B., Third, J.R., Müller, C. R., *Discrete element models for non-spherical particle systems: From theoretical developments to applications*. Chemical Engineering Science, 2015. https://doi.org/10.1016/j.ces.2014.11.050

[23] Radl, S., Sundaresan, S., *A drag model for filtered Euler-Lagrange simulations of clustered gas-particle suspensions*. Chemical Engineering Science, 2014. **117**: p. 416-425. https://doi.org/10.1016/j.ces.2014.07.011

[24] Wu, H., et al., *Parameter analysis and wall effect of radiative heat transfer for CFD-DEM simulation in nuclear packed pebble bed*. ECMF, 2020. **3**: p. 250-257. https://doi.org/10.1007/s42757-020-0058-2.

[25] Wang, J., Li, J., Zhang, Y., *CFD-DEM investigation of particle-scale heat transfer mechanisms in fluidized beds*. International Journal of Heat Mass Transfer, 2021. **171**: p. 121-130.

[26] Wang, S., Luo, K., Hu, C., Lin, J., Fan, J., "CFD-DEM simulation of heat transfer in fluidized beds: Model verification, validation, and application," Chemical Engineering Science, 2019. **197**:p.280-295. https://doi.org/10.1016/j.ces.2018.12.031

[27] Xu, Y., Yang, N., Li, J., "*CFD-DEM simulation of heat transfer in particulate systems*," International Journal of Heat Mass Transfer, 2020. **149**: 119170.

[28] Zhu, H.P., Zhou, Z.Y., Yang, R.Y., Yu, A.B., *Discrete particle simulation of particulate systems: Theoretical developments*. Chemical Engineering Science, 2007. **62** (13): p. 3378-3396, https://doi.org/10.1016/j.ces.2006.12.089

[29] Baltussen, M.W., Buist, K.A., Peters, E.A.J.F., Kuipers, J.A.M., *Multiscale modelling of dense gas-particle flows*. Advance Chemical Engineering, 2018. **53**: p.1-52. https://doi.org/10.1016/bs.ache.2018.02.001.

[30] Shuai, W., Kun, L., Chenshu, H., Junjie, L., Jianren, F., *CFD-DEM Simulation of Heat Transfer in Fluidized Beds: Model Verification, Validation, and Application*. Chemical Engineering Journal, 2019. https://doi.org/10.1016/j.ces.2018.12.031.

[31] Adapa, R. S., Zhang, X., Feng, T., Man Chung, K., Albrecht, J. K., Ho, K. C., Madden, A. D., Chen, R., *Heat transfer coefficients of moving particle beds from flow-dependent thermal conductivity and near-wall resistance*. Solar Energy, 2024. **282**, 112960. https://doi.org/10.1016/j.solener.2024.112960.

[32] Subburaj, R., Tang, Y., Deen, N. G., "Euler-Lagrange Simulations of Microstructured Bubble Columns Using a Novel Cutting Model," Industrial & Engineering Chemical Research,

2023. **62** (38): p. 15656-15665. DOI:10.1021/acs.iecr.3c02352.

[33] Handayani, S., Wahyudi, H., Agustina, S., Yulianto, M., Ariyanto, H., *CFD-DEM Study of heat and mass transfer of ellipsoidal particles in fluidized bed dryers*, Powder Technology, 2023. **425**: 118535 https://doi.org/10.1016/j.powtec.2023.118535

[34] de Munck, M.J.A., Peters, E.A.J.F., Kuipers, J.A.M., "*CFD-DEM modeling and validation of solids drying in a gas-fluidized bed*. Chemical Engineering Science, 2024. **291**:119922. https://doi.org/10.1016/j.ces.2024.119922.

[35] de Munck, M.J.A., Peters, E.A.J.F., Kuipers, J.A.M., *Fluidized bed gas-solid heat transfer using a CFD-DEM coarse-graining technique*. Chemical Engineering Science, 2023. **280**: 119048. https://doi.org/10.1016/j.ces.2023.119048

[36] You, J., Wang, C., Fan, Y., *Numerical study of particle-scale heat transfer in fluidized beds using CFD-DEM*, Chemical Engineering Science, 2019. 195: p. 674-685.

[37] Hoorijani, H., Esgandari, B., Zarghami, R., Gharebagh, R., Mostoufi, N., *CFD-DEM simulation of heat transfer in spout-fluid beds*. Chemical Engineering Research and Design, 2023. **200**: p. 95-106. https://doi.org/10.1016/j.cherd.2023.10.030

[38] Alipoor, M., Zarghami, R., Mostoufi, N., "*CFD-DEM investigation of the effects of particle size and fluidization regime on heat transfer in fluidized beds*. Computational Particle Mechanics, 2025. **12**(4): p. 2037-2058. https://doi.org/10.1007/s40571-025-01018-8.

[39] Glicksman, L.R., *Scaling relationships for fluidized beds*. Powder Technology, 1984. **40**: p.17-36.

[40] Mu, L., Liu, Y., Zhong, W., Wang, Q., *Numerical investigation on heat transfer in a pseudo-2D fluidized bed using CFD-DEM*. Processes, 2020. **8**: 463.

[41] Sharif, S., Shakaib, M., Usman, A. *A CFD and experimental study of hydrodynamic and heat transfer behavior in ribbed fluidized beds*. International Journal of Chemical Reactor Engineering, 2024. **22**(9): p. 1039-1054. https://doi.org/10.1515/ijcre-2024-0052

[42] Cúñez, F., Lima, N., Franklin, E., *Motion and clustering of bonded particles in narrow solid-liquid fluidized beds*. Physic Fluids, 2021. **33**: 023303. https://doi.org/10.1063/5.0035718

[43] Xu, Y., Wang, Q., Yang, N., Jin, Y., *CFD-DEM modeling the effect of column size and bed height on minimum fluidization velocity in micro fluidized beds with Geldart B particles*. Powder Technology, 2017. DOI: 10.1016/j.powtec.2017.06.020.

[44] Al-Arkawazi, S., Marie, C., Benhabib, K., Coorevits, P., *Modeling the hydrodynamic forces between fluid-granular medium by coupling DEM-CFD*. Chemical Engineering Research and Design, 2017. **117**: p.439-447. https://doi.org/10.1016/j.cherd.2016.11.002.

[45] Sherko Ahmad Flamarz, *Computational Study of Heat Transfer Behavior in Fluid-Solid Fluidized Beds*. Sulaimani Journal for Engineering Sciences, 2020. **7** (3): p.35-45. https://doi.org/10.17656/sjes.10132.

[46] Launder, B. E., Spalding, D. B., *The numerical computation of turbulent flows*. Computer Methods in Applied Mechanics and Engineering, 1974. **3**(2): p. 269-289.

[47] Archambeau, F., Méchitoua, N., Sakiz, M., *Code Saturne: A Finite Volume Code for the computation of turbulent incompressible flows - Industrial Applications*. International Journal on Finite Volumes, 2004. **1**(1): p.1-62.

[48] Cundall, P. A., Strack, O. D. L., "*A discrete numerical model for granular assemblies*," Geotechnique, 1979. **29** (1): p. 47-65. https://doi.org/10.1680/geot.1979.29.1.47.

[49] Jean, M., Moreau, J.J., *Unilaterality and dry friction in the dynamics of rigid body collections. In: Curnier, A. (Ed.)*. 1992, Proc. Contact Mechanics Int. Symp., Edt. A. Curnier, PPUR, 31-48.

[50] Fortin, J., De Saxcé, G., *Modélisation numérique des milieux granulaires par l'approche du bi-potentiel*. Comptes Rendus de l'Académie des Sciences - Series IIB - Mechanics-Physics-Astronomy, 1999. **327**: p.721-724.

[51] Fortin, J., Coorevits, P., *Selecting contact particles in dynamics granular mechanics systems*. Journal of Computational Applied Mathematics, 2004. **168**: p. 207-213.

[52] Mindlin, R. D., Deresiewicz, H., *Elastic Spheres in Contact under Varying Oblique Forces*. Journal Applied Mechanics, 1953. **20**: p. 327-344.

[53] Di Felice, R., *The voidage function for fluid-particle interaction systems*. International Journal of Multiphase Flow, 1994. **20**(1): p. 153-159. https://doi.org/10.1016/0301-9322(94)90011-6.

[54] Syamlal, M., Rogers, W., O'Brien, T. J., "*MFIX Documentation: Theory Guide. U.S. Department of Energy*. 1993, Morgantown Energy Technology Center.

[55] Zhao, Y., Jiang, M., Liu, Y., Zheng, J., *Particle-scale simulation of the flow and heat transfer behaviors in a fluidized bed with an immersed tube*. Aiche Journal, 2009. **55**(12): p. 3109-3124. DOI: 10.1002/aic.11956

[56] Zabrodsky, S.S., *Hydrodynamics and Heat Transfer in Fluidized Beds*. 1966, M.I.T Press, Cambridge, Massachusetts.

[57] M. Barigou, S. Mankad, P. J. Fryer, *Heat transfer in two-phase solid-liquid food flows: A review*. Food Bioproduction Process, 1998. https://doi.org/10.1205/096030898531710.

[58] Incropera, F.P., DeWitt, D.P., Bergman, T.L., Lavine, A.S., *Fundamentals of Heat and Mass Transfer*. 2017, 8th ed., Wiley.

[59] Bird, R.B., Stewart, W.E., Lightfoot, E.N., *Transport Phenomena*. 2002, 2nd ed., Wiley.

[60] Holman, J.P., *Heat Transfer*, 2010. 10th ed., McGraw-Hill.

[61] Batchelor, G. K., O'Brien, R. W., *Thermal or electrical conduction through a granular material*. Proceedings of the Royal Society of London. Series A, Mathematical and Physical Sciences, 1977. **355** (1682): p.313-333. https://doi.org/10.1098/rspa.1977.0100

[62] Al-Arkawazi, S., *Modélisation des interactions fluide-milieu granulaire par couplage CFD-DEM, incluant les transferts thermiques*. Thèse de doctorat, Sciences, Technologies et Santé, Université de Picardie Jules Verne, 2014.

[63] Sherko Ahmad Flamarz, *Simulating the heat transfer behavior in a fluidized bed by a combined thermal model in the CFD-DEM coupling*. 9th Scientific Conference of University of Garmian, Special issue for Passer Journal of basic and applied science, 2022. **4**:p.205-219. DOI: 10.24271/PSR.2022.161697

[64] Jaćimovski, D. R., Brzić, D. V., Garić-Grulović, R. V., Pjanović, R. V., Đuriš, M. M., Arsenijević, Z. J., Bošković-Vragolović, N. M., *Heat transfer by liquid convection in particulate fluidized beds*. Journal Serbian Chemical Society, 2022. **87** (7-8): p. 911-924. doi.org/10.2298/JSC211216020J

[65] Gunn, D.J., *Transfer of heat or mass to particles in fixed and fluidized beds*. International Journal of Heat Mass Transfer, 1978. **21**: p.467-476. https://doi.org/10.1016/0017-9310(78)90080-7.

[65] Wen, C.Y., Yu, Y.H., *A generalized method for predicting the minimum fluidization velocity*. AIChE Journal, 1966. **12**: p. 610-612. https://doi.org/10.1002/aic.690120343.

دور المعايير الهندسية في انتقال الحرارة في طبقات التمييع السائلة الصلبة

المستخلص

ان فهم كيفية انتقال الحرارة في الأسرّة المميَّعة سائل– صلب أمر بالغ الأهمية لتحسين تصميم أنظمة المعالجة الكيميائية والحرارية. تم إجراء تحقيق عددي لدراسة الخصائص الهيدروديناميكية وانتقال الحرارة في الأسرّة المميَّعة سائل– صلب باستخدام نهج مقترن بين (CFD–DEM) مدمج مع نموذج حراري. استُخدم هذا الاقتران لتقييم كيفية أنتقال الحرارة عبر ثلاثة أقطار مختلفة للجسيمات وقطرين مختلفين للعمود، وذلك ضمن مدى من سرعات المائع، بهدف دراسة تأثير المعاملات الهندسية والظروف الهيدروديناميكية على انتقال الحرارة. تم الحفاظ على درجة حرارة جدار الدخول عند قيمة ثابتة، بينما تم إبقاء الجدران الأخرى في حالة من التساوي الحراري، من أجل محاكاة شروط الحدود الحرارية الموجودة في التطبيقات الصناعية. وقد وجد أن الجسيمات الصغيرة توفر مساحة أكبر للاتصال وتزيد من معدل انتقال الحرارة. كما لوحظ تحسن في أنتقال الحرارة بالحمل وتقلّل من تدرّج درجات الحرارة داخل السرير مع زيادة سرعة المائع الداخل، خاصة في الأعمدة ذات الأقطار الكبيرة. أظهرت النتائج أن انتقال الحرارة يحدث بالتوصيل في نقاط التماس بين الجسيمات، وعبر الحمل بين المائع والجسيمات، وأظهرت أن التفاعل بين حجم الجسيم وقطر العمود وسرعة المائع تؤثرعلى أداء عملية نقل الحرارة. أُجريت مقارنات بين النتائج العددية الحالية والبيانات التجريبية المتاحة في الأدبيات لكل من السلوك الهيدروديناميكي والحراري، وأظهرت توافقًا جيدًا مع النتائج التجريبية المنشورة. وتوفّر هذه النتائج إرشادات لتحسين هندسة الأعمدة وحجم الجسيمات في مفاعلات الأسرّة المميَّعة من أجل تعزيز الكفاءة الحرارية في معدات المعالجة الكيميائية والحرارية.

الكلمات المفتاحية:

انتقال الحرارة ، التمييع ، طبقات معبأة ، قطر العمود

Table 1. Physical properties of the material in bed.

Particle property (Glass beads)	Value
Particle diameter, d_p [mm]	2.0
Column diameters investigated [mm]	96.0
Bed height (initial) [mm]	100
Density, ρ_p [kg/m^3]	2450
Coefficient of friction, μ_s [-]	0.30
Young's modulus, E [GPa]	70.0
Poisson's ratio, ν [-]	0.35
Time step for fluidized bed, Δt [s]	5*10^{-5}
Simulation time [s]	10.0

Table 2. Physical properties for the Particle and the Fluid

Particle and Fluid properties	Value
Particle diameter, d_p [mm]	2, 3, 5
Density, ρ_p [kg/m^3]	2700
Thermal conductivity λ_p [W/(m.K)]	237
Heat capacity, C_p [J/(kg.K)]	900
Coefficient of friction, μ_s [-]	0.30
Poisson's ratio, ν [-]	0.35
Young's modulus, E [GPa]	69.0
Column diameters investigated [mm]	51, 96
Bed height (initial) [mm]	100
Time step for fluidized bed, Δt [s]	5*10^{-5}
Initial temperature, T_f [K]	293.15
Density, ρ_f [kg/m^3]	1000
Viscosity μ_f [kg/m.s]	0.001
Heat capacity, C_f [J/(kg.K)]	4200
Thermal conductivity, λ_f [W/(m.K)]	0.60

Table 3. Properties of meshes for two column diameters

Column diameter	Tetrahedrons	Nodes	Edges	Triangles	Mesh size
51 mm	3710	1122	92	1712	(0.0312-0.07237)
96 mm	2464	766	69	1210	(0.0301-0.07329)

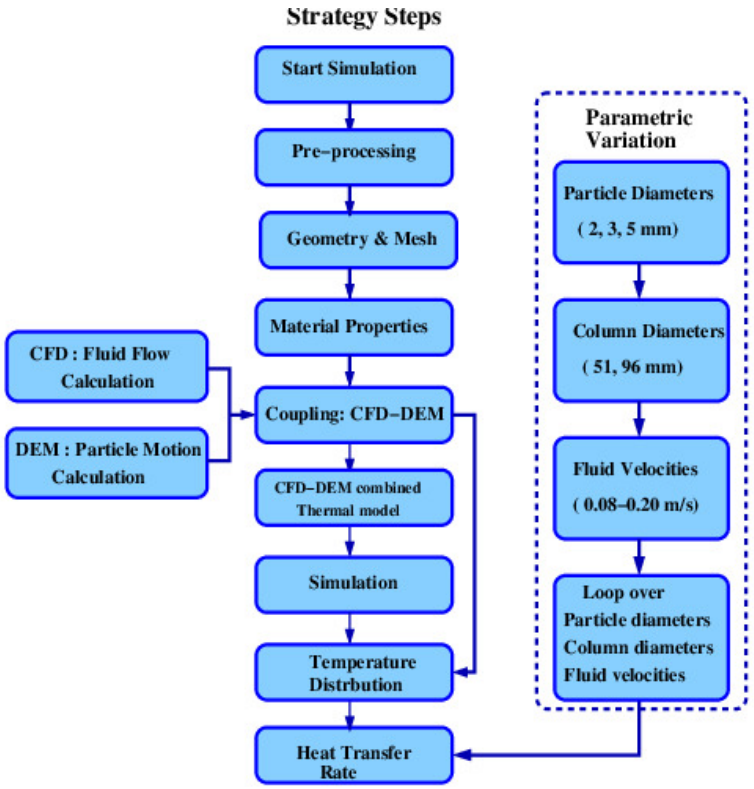

Figure1. Flow chart of the CFD-DEM approach to the simulation of heat transfer in a liquid-solid fluidized bed.

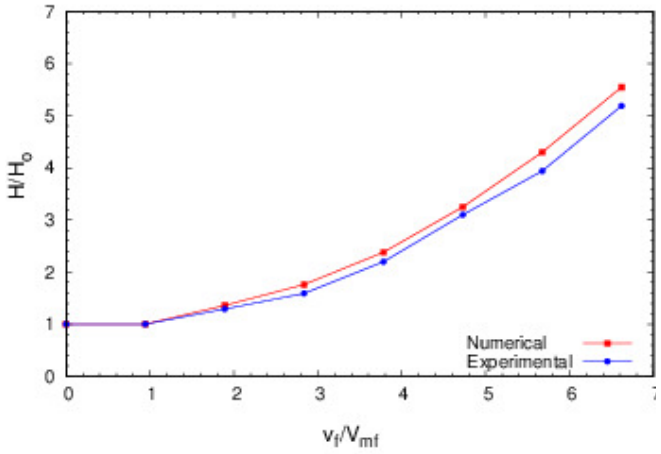

Figure 2. Comparison between the numerical and experimental findings in terms of maximum expansion ratio (H/H_o) with the velocity ratio (v_f/V_{mf}).

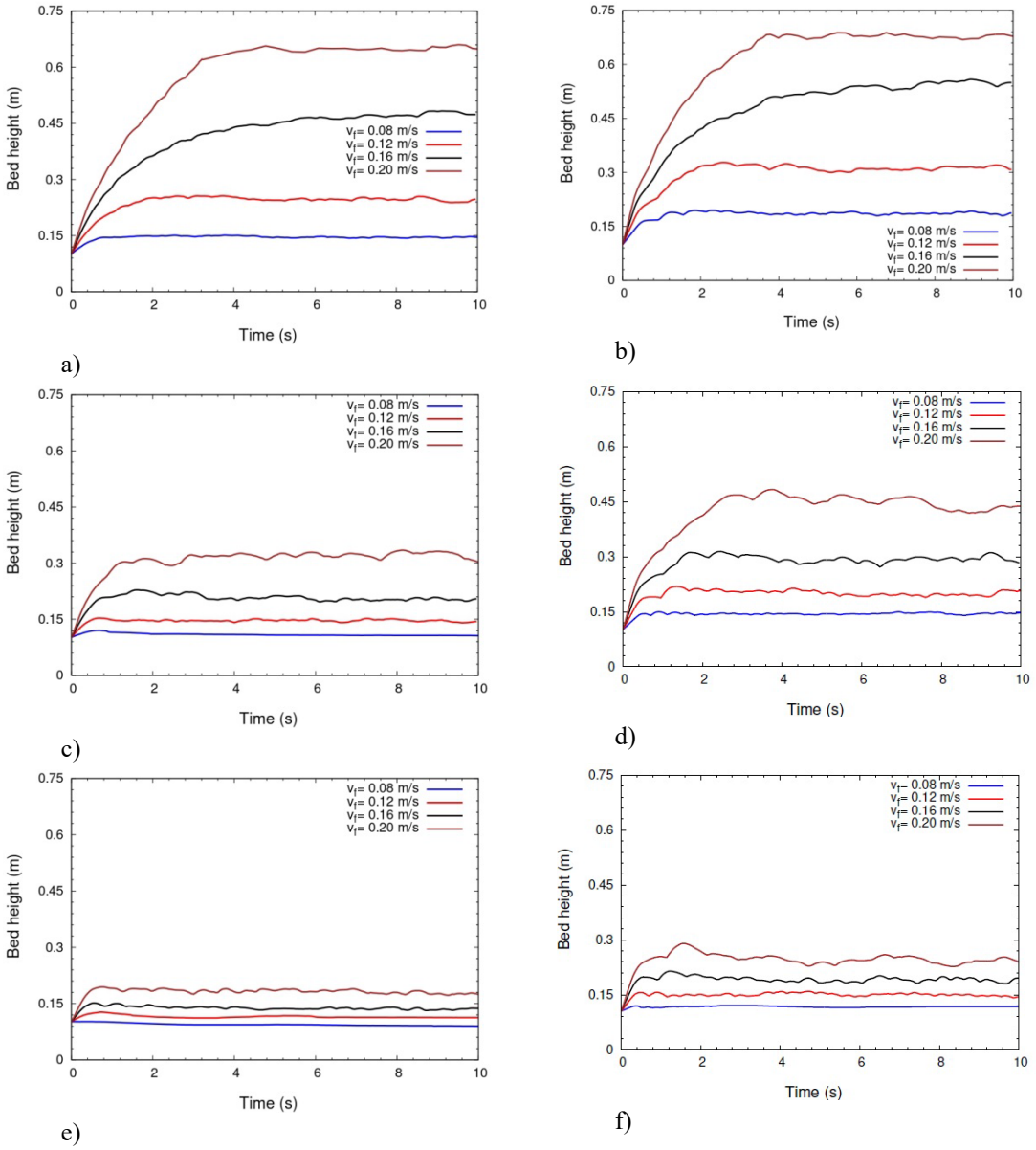

Figure 3. Comparison of bed height evolution with time for column inner diameter; for D = 51 mm with a) d_p = 2 mm, c) d_p =3 mm, e) d_p = 5 mm, and D = 96 mm with b) d_p = 2 mm, d) d_p =3 mm, and f) d_p = 5 mm.

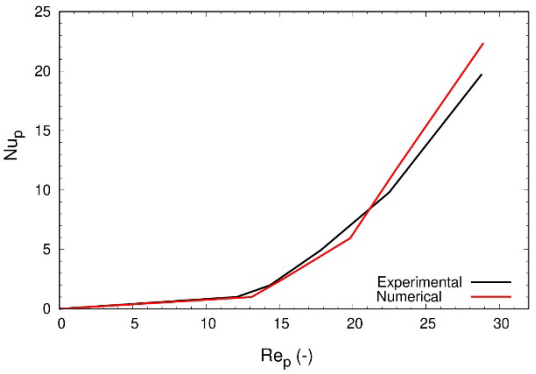

Figure 4. Comparison between the numerical and experimental findings in terms of particle Nusselt number (Nu_p) and particle Reynolds number (Re_p).

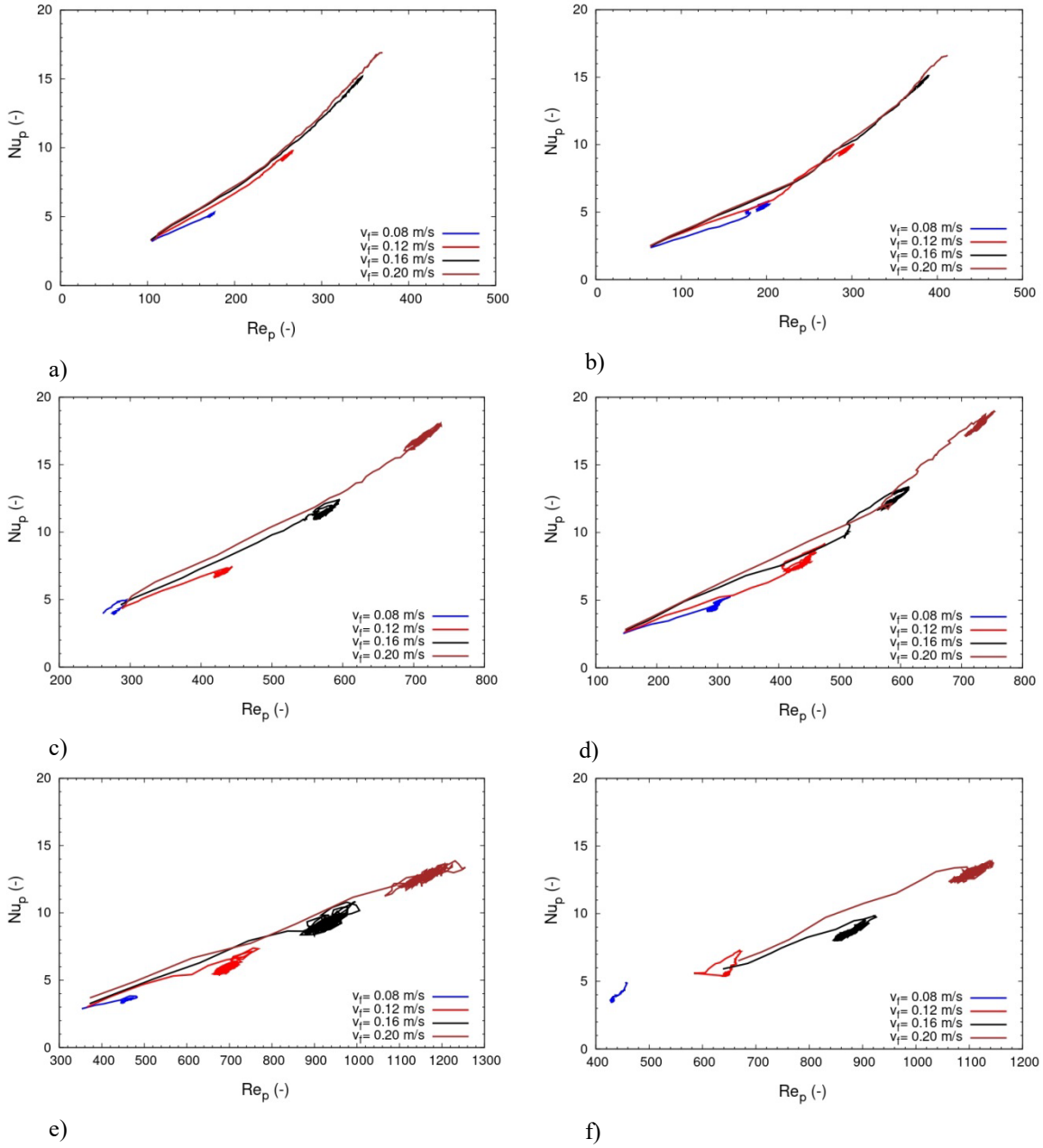

Figure 5. Correlation between particle Nusselt number (Nu_p) and particle Reynolds number (Re_p) for all tested particle sizes and column diameter, where, for D = 51 mm, with a) d_p = 2 mm, c) d_p =3 mm, e) d_p = 5 mm, and D = 96 mm with b) d_p = 2 mm, d) d_p =3 mm, and f) d_p = 5 mm.

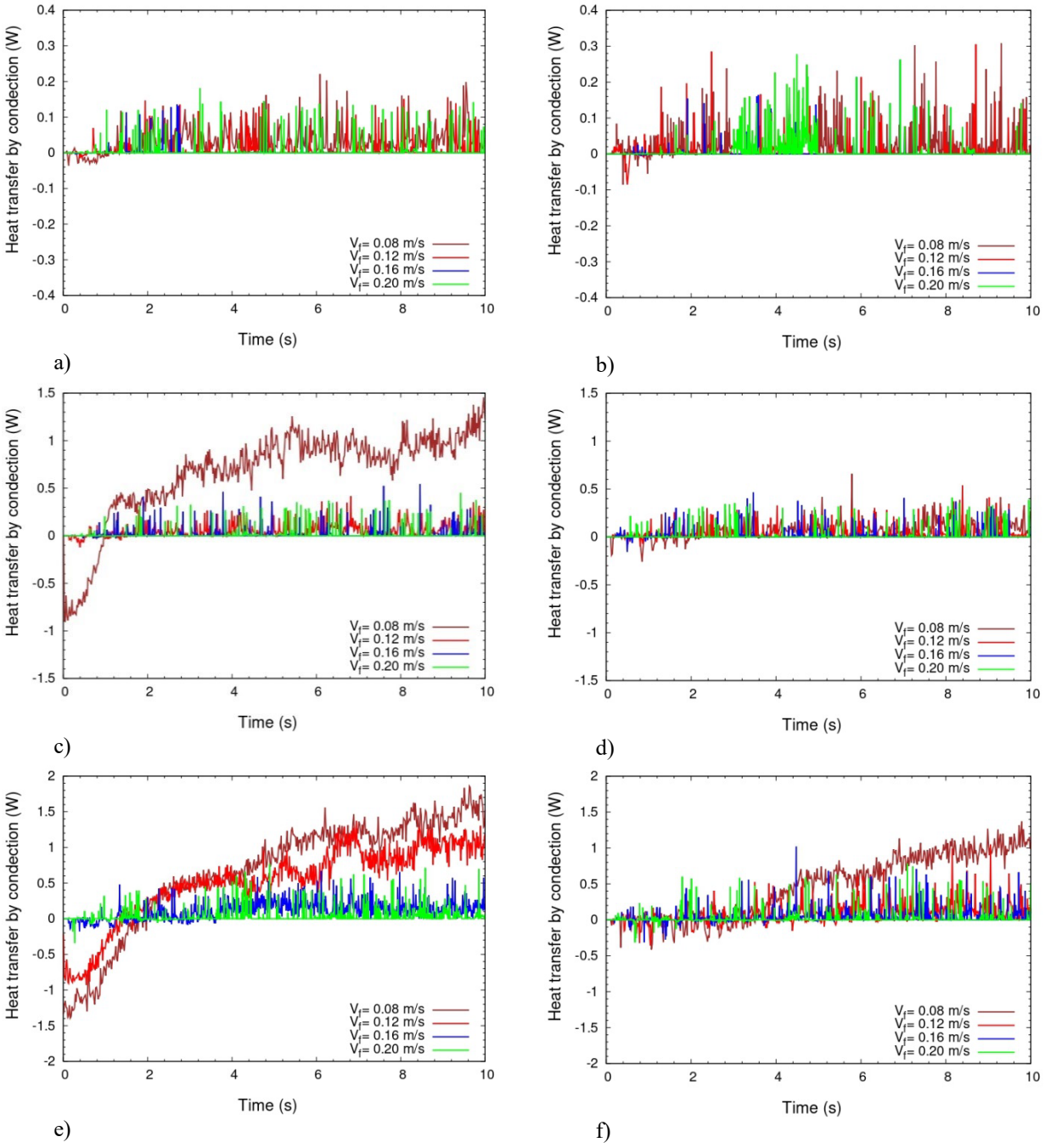

Figure 6. Variation of heat transfer by conduction with time. For D = 51 mm with a) d_p = 2 mm, c) d_p =3 mm, e) d_p = 5 mm, and D = 96 mm with b) d_p = 2 mm, d) d_p =3 mm, and f) d_p = 5 mm.

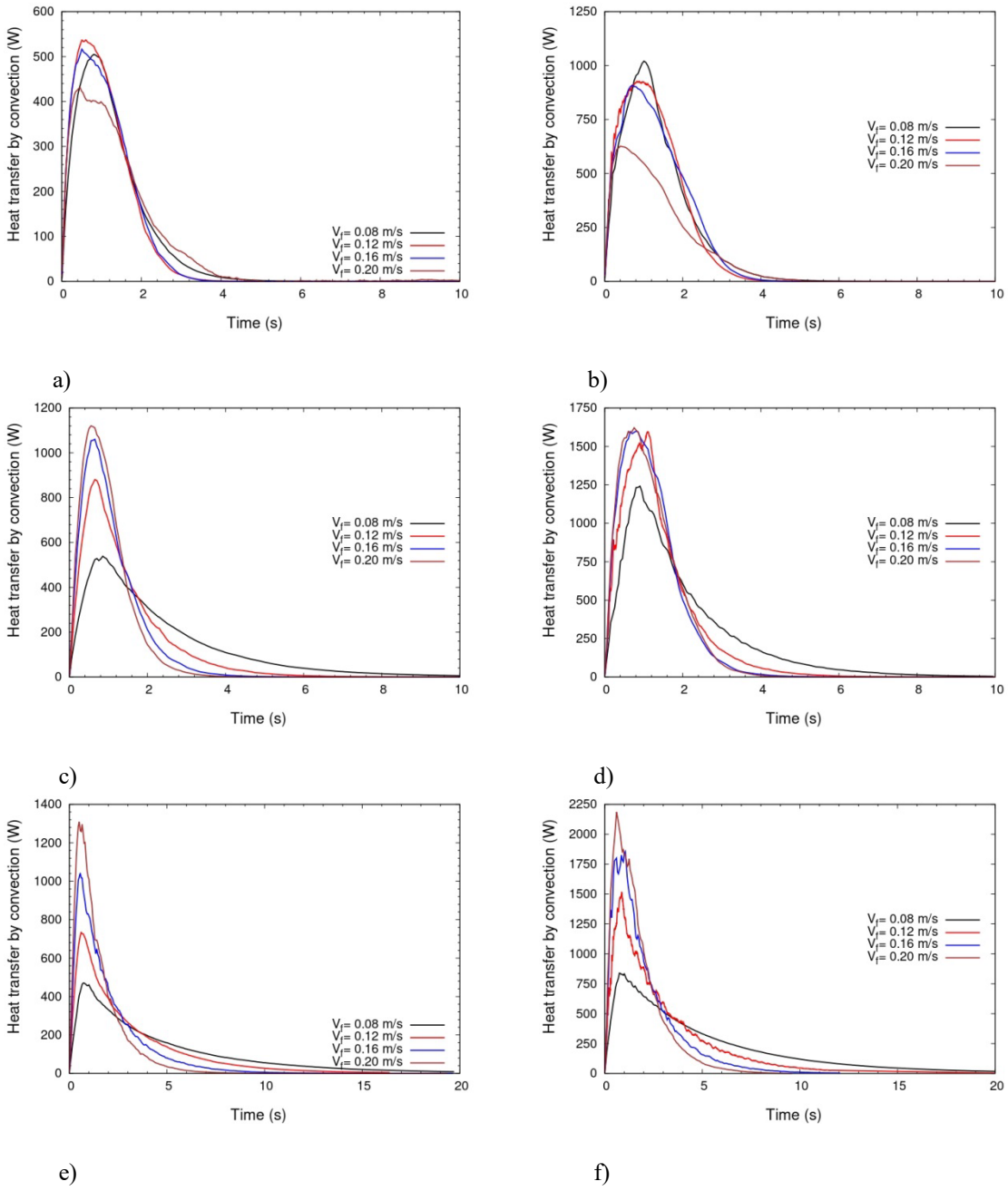

Figure 7. Variation of heat transfer by convection with time. For D = 51 mm with a) d_p = 2 mm, c) d_p =3 mm, e) d_p = 5 mm, and D = 96 mm with b) d_p = 2 mm, d) d_p =3 mm, and f) d_p = 5 mm.

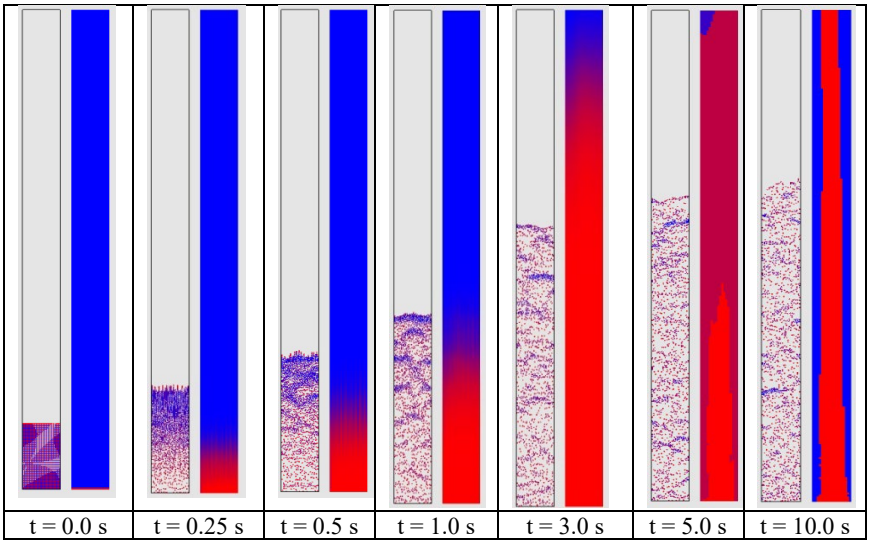

a) Column inner diameter (D = 51 mm) and particle diameter (d_p = 2 mm).

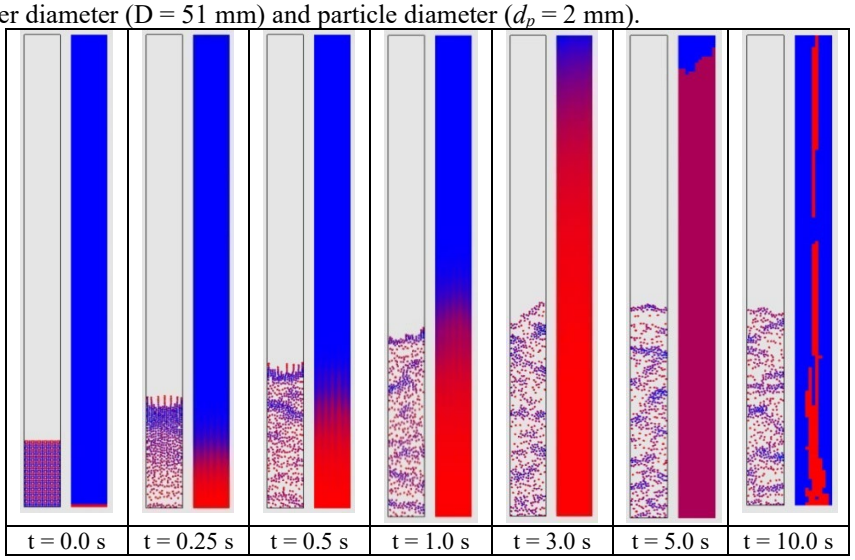

b) Column inner diameter (D = 51 mm) and particle diameter (d_p = 3 mm).

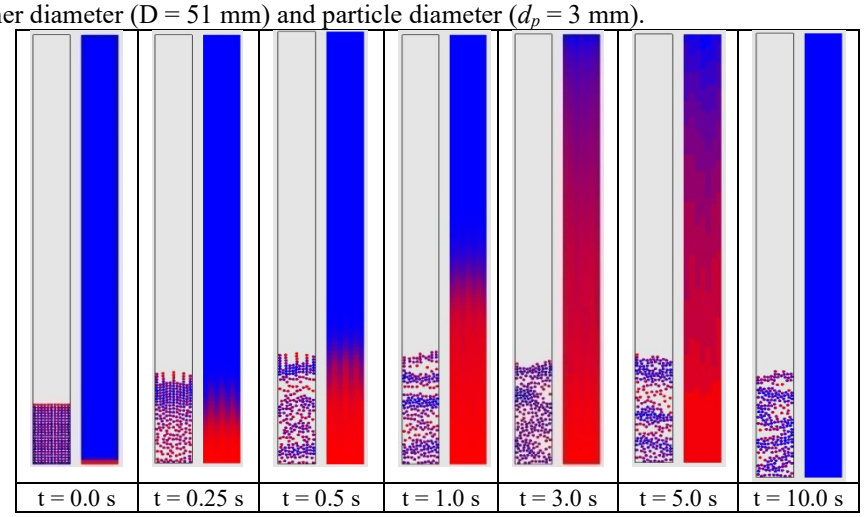

c) Column inner diameter (D = 51 mm) and particle diameter (d_p = 5 mm).

Figure 8. Temporal snapshots of the heating process in a liquid-solid fluidized bed (D = 51 mm) operating with an inlet fluid velocity of 0.20 m /s and an inlet wall temperature of 90 °C. The evolution of temperature and particle mixing is demonstrated for particle diameters of: a) 2 mm, b) 3 mm and c) 5 mm.

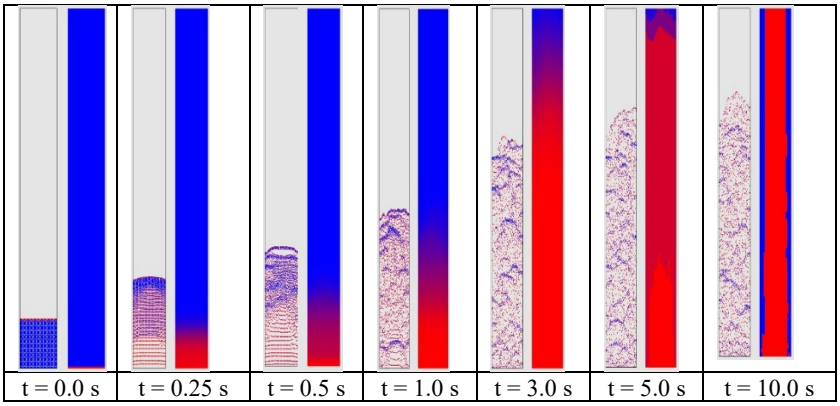

a) Column inner diameter (D = 96 mm) and particle diameter (d_p = 2 mm).

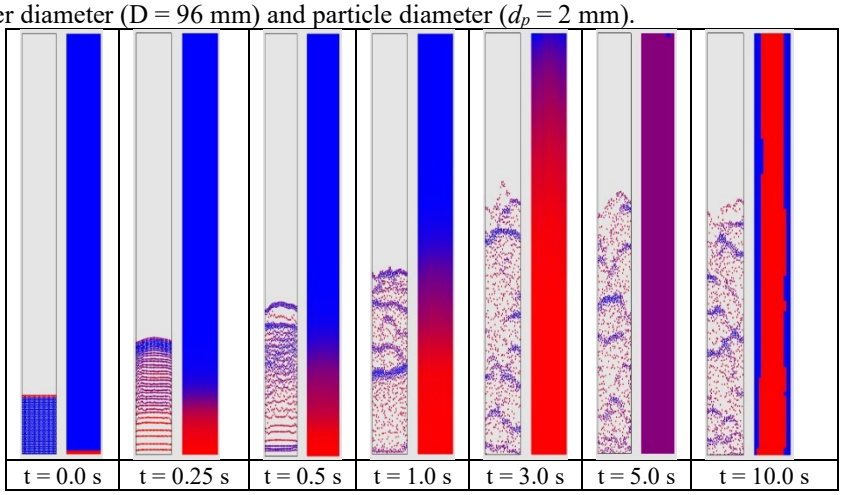

b) Column inner diameter (D = 96 mm) and particle diameter (d_p = 3 mm).

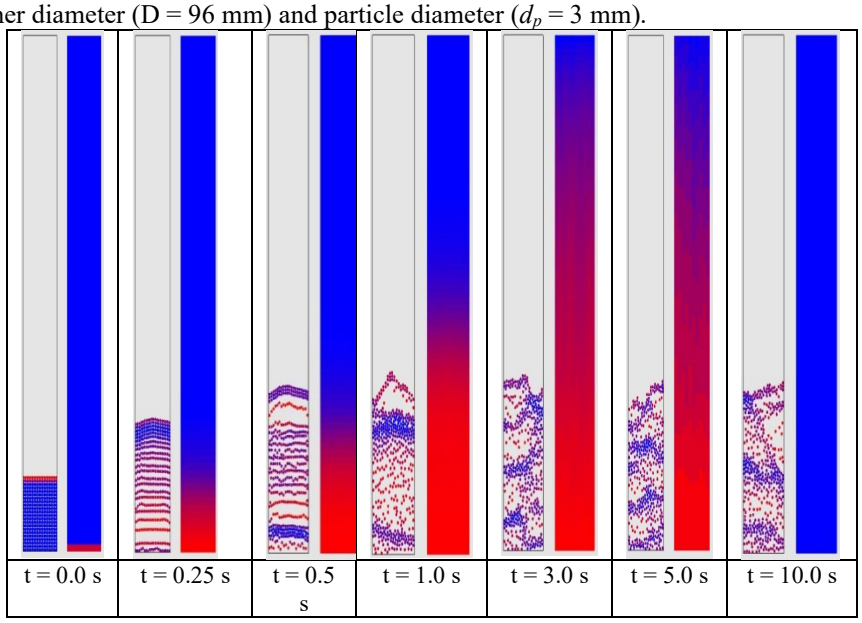

c) Column inner diameter (D = 96 mm) and particle diameter (d_p = 5 mm).

Figure 9. Temporal snapshots of the heating process in a liquid-solid fluidized bed (D = 96 mm) operating with an inlet fluid velocity of 0.20 m /s and an inlet wall temperature of 90 °C. The evolution of temperature and particle mixing is demonstrated for particle diameters of: a) 2 mm, b) 3 mm and c) 5 mm.